

National Chiao Tung University

Department of Applied Chemistry

PhD Thesis

**Raman Micro-spectroscopic and Imaging Studies of
Escherichia coli Biofilm *in situ* and Intracellular
Dynamics of Fission Yeasts *in vivo* Using Stable
Isotope Labelling**

The logo of National Chiao Tung University is a circular emblem with a gear-like border. Inside the circle, there is a stylized building and the year '1896' at the bottom.

Student: Hemanth Nag Noothalapati Venkata


Advisor: Dr. Shinsuke Shigeto

July 2013

Raman Micro-spectroscopic and Imaging Studies of *Escherichia coli* Biofilm *in situ* and Intracellular Dynamics of Fission Yeasts *in vivo* Using Stable Isotope Labelling

Student: Hemanth Nag Noothalapati Venkata

Advisor: Dr. Shinsuke Shigeto

The logo of National Chiao Tung University is a circular emblem with a gear-like outer border. Inside the circle, there is a stylized building and the letters 'ES' and 'A' are visible. The year '1896' is at the bottom of the emblem.

A Thesis
Submitted to Ph. D. Program, Department of Applied Chemistry
College of Science
National Chiao Tung University
in Partial Fulfillment of the Requirements
for the Degree of Doctor of philosophy
in
Applied Chemistry

July 2013

Hsinchu, Taiwan, Republic of China

Raman Micro-spectroscopic and Imaging Studies of *Escherichia coli* Biofilm *in situ* and Intracellular Dynamics of Fission Yeasts *in vivo* Using Stable Isotope Labelling

Student: Hemanth Nag Noothalapati Venkata

Advisor: Dr. Shinsuke Shigeto

Ph. D. Program, Department of Applied Chemistry

National Chiao Tung University



Biological processes have intricate designs by nature. The main purpose of this work is to decode some of these designs. Many areas in biology including studies on microbial communities and cellular biochemistry still largely remain unexplored due primarily to the lack of appropriate tools. In this thesis, we present the applications of Raman micro-spectroscopy and imaging to gain fundamental and otherwise unobtainable biological information on complex structured communities of bacteria known as biofilms and on the metabolic dynamics in single yeast cells.

To demonstrate the power of Raman spectroscopy for complex biological systems, model *Escherichia coli* biofilms were studied. A variety of biomolecules have been shown to play a unique role as signals and/or regulators in biofilm formation. By using Raman imaging, we investigated model *Escherichia coli* biofilms and detected high levels of the amino acid

leucine (leucine pool) have been detected, for the first time, within micro-colonies in a nascent *E.coli* biofilm. Localization of leucine revealed by multi-frequency Raman images indicates leucine accumulation during the early stage of the *E. coli* biofilm formation, which may have resulted from physiological environment-specific metabolic adaptation. Our results demonstrates that our label-free Raman imaging method provides a useful platform for directly identifying still unknown natural products produced in biofilms as well as for visualizing heterogeneous distributions of biofilm constituents *in situ*.

To elucidate the dynamics of intracellular proteins and lipids at the single cell level, the Raman method was coupled with a very powerful strategy, namely, stable isotope labelling. Here, we present *in vivo* time lapse Raman imaging, coupled with stable-isotope (^{13}C) labelling, of single living *Schizosaccharomyces pombe* cells. Lipid droplets have been hypothesized to be intimately associated with intracellular proteins. However, there is little direct evidence for both spatiotemporal and functional relations between lipid droplets and proteins provided by molecular-level studies on intact cells. Using characteristic Raman bands of proteins and lipids, the process by which ^{13}C -glucose in the medium was assimilated into those intracellular components was dynamically visualized. Our results show that the proteins newly synthesized from incorporated ^{13}C -substrate are localized specifically to lipid droplets as the lipid concentration within the cell increases. We demonstrate that the present method offers a unique platform for proteome visualization without the need for tagging individual proteins with fluorescent probes.

Finally, in chapter V we conclude by summarizing what has been achieved during this thesis work and also present a possible new direction of study in the future with our method..

Acknowledgements

First, I would like to express my sincere gratitude to Profs. Hiro-o-Hamaguchi and Shinsuke Shigeto for giving me an opportunity, for their stimulating discussions, and for their constant support throughout this work. Honestly, it would not have been possible to finish my thesis without the help from so many people but to only some of whom it is possible to give a particular mention here.

I must specially thank my supervisor Prof. Shinsuke Shigeto for his faith in me that I can carry out this work, for his continuous and thoughtful guidance, for being patient, understanding and supportive in those times when there was not much progress.

My thanks to Dr.Soshi Yabumoto for his active discussions, arguments and for teaching some basic things during my first two years. I am indebted to Dr. Chuan-Keng Huang and to many students from the Hamaguchi group Drs. Chikao Onogi, Masahiro Ando, Rintaro Shimada, Venkatesh Kaliaperumal, Liang-da Chiu for their stimulating discussions and valuable suggestions.

My thanks to all the past and present members of the Shigeto group for their kind help, which made my stay in Taiwan comfortable. I would also like to thank Ministry of Education, Taiwan for the fellowship during the first three years of my study.

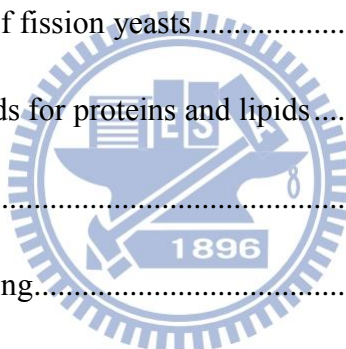
This acknowledgement would be incomplete without expressing my heartfelt thanks to Mr. Sudhakar Narra and Prof. Satyen Saha for their invaluable support both professionally and personally.

Last but not the least, I am deeply thankful to my family and friends for their continuous encouragement and support throughout. I would like to dedicate this thesis to my late grandmother and late aunt who continue to inspire me in every possible way.

Table of Contents

Abstract.....	i
Acknowledgements	iii
Table of Contents.....	iv
List of Figures.....	vi
List of Tables	viii
Chapter I Introduction	1
Chapter II Experiment and Data Analysis	6
II-1. Confocal Raman micro-spectrometer.....	7
II-2. Estimation of lateral and axial resolutions	9
II-3. Singular value decomposition analysis.....	10
Chapter III Detection of Leucine Pools in <i>Escherichia coli</i> Biofilm.....	15
III-1. Introduction	16
III-2. What are biofilms?	17
III-3. Developmental stages in biofilms	18
III-4. General methods to study biofilms.....	19
III-5. <i>Escherichia coli</i>	20
III-6. Raman spectrum of a single planktonic <i>E. coli</i>	20
III-7. Space-resolved Raman spectra of <i>E. coli</i> biofilms.....	23
III-8. Raman imaging of a single microcolony	28
III-9. Three dimensional (3D) Raman imaging.....	30

III-10. Why leucine?	30
III-11. Conclusion.....	32
Chapter IV Visualization of Dynamic Proteome Localization to Lipid Droplets in Single Fission Yeast Cells Using Stable Isotope Probing	33
IV-1. Introduction	34
IV-2. How can Raman microspectroscopy help?	35
IV-3. Stable isotope probing.....	36
IV-4. Sample.....	37
IV-5. Growth of yeast cells in ¹³ C medium	39
IV-6. Stable isotope labeling of fission yeasts.....	40
IV-7. Selection of marker bands for proteins and lipids.....	43
IV-8. Bulk experiments.....	44
IV-9. Single cell Raman imaging.....	50
IV-10. Biological implications of this colocalization phenomenon	56
IV-11. Conclusion.....	57
Chapter V Summary and Future Perspectives	58
References	60



List of Figures

Figure II-1. Schematic representation of our laboratory-built confocal Raman micro-spectrometer.....	8
Figure II-2. Evaluation of (a) lateral and (b) axial resolution of our laboratory built confocal Raman micro-spectrometer.....	10
Figure II-3. Principle of SVD.....	11
Figure II-4. Graphical representation of SVD.....	12
Figure II-5. (a) Optical image of a typical fission yeast cell; (b,c) Raman images constructed for 1602 cm ⁻¹ with raw data before SVD (b) and after SVD analysis (c); and (d) representative space-resolved Raman spectra from the same data which were acquired with an exposure time of 1.5 s and 1 mW laser power.	14
Figure III-1. Developmental stages of a biofilm.....	18
Figure III-2. Scanning electron micrograph of <i>E.coli</i> grown in culture medium and adhered to a cover slip.....	20
Figure III-3. Typical Raman spectrum of a single <i>E. coli</i> bacterium, with 632.8 nm excitation, optically trapped at the focal point.	21
Figure III-4. Optical micrograph of a 30-hour old biofilm.....	25
Figure III-5. (a) Optical micrograph of a single microcolony in 30 h old biofilm on which further experiments were done. Space-resolved Raman spectra of the 30-h old <i>E.coli</i> biofilm (b) intracolony, (c) extracolony and (d) a planktonic <i>E.coli</i> cell. Stars denote the positions at which (b) and (c) are recorded.....	26
Figure III-6. Comparison of (a) intracolony Raman spectrum with those of crystalline (b) L-leucine, (c) L-isoleucine and (d) L-valine	27
Figure III-7. (a) Optical micrograph of the scanned region and Raman images of the 30-h-old <i>E. coli</i> biofilm of the Raman bands at (b) 1097, (c) 782, (d) 1408, (e) 1130, (f) 922, (g) 847, (h) 671, and (i) 533 cm ⁻¹ . Images (b) and (c) represent the DNA distribution, while images (d)–(i)	

represent the leucine distribution.....	29
Figure III-8. Raman sectioning of the 30-hour-old <i>E. coli</i> biofilm Z stacks of the Raman images at (a) 782 cm ⁻¹ (the O–P–O symmetric stretch plus contributions of cytosine and thymine vibrational modes), (b) 922, and (c) 1408 cm ⁻¹	31
Figure IV-1. Schematic representation of a lipid droplet.	34
Figure IV-2. Illustration of isotope-induced red shift in a Raman	37
Figure IV-3. Scanning electron micrograph of a fission yeast (<i>S.pombe</i>) culture.....	38
Figure IV-4. Growth curves of fission yeast in ¹² C- and ¹³ C-glucose containing Edinburgh minimal medium.....	39
Figure IV-5. (a) Optical image of a typical fission yeast. The transparent region inside the cell indicated by an asterisk is the cytoplasm where protein rich spectra were recorded. The black dot, highlighted by a shown in red square represents LD where lipid rich spectra were measured. Scale bar = 5μm. (b,c) Space-resolved Raman spectra from yeast grown in ¹² C and ¹³ C-EMM in protein rich (b) and lipid rich regions (c) to identify vibrational isotope shifts.	41
Figure IV-6. (a) Space- and time-resolved Raman spectra showing the evolution of isotope incorporation in PR regions in yeasts, (b) Percentage similarity among PR spectra at each time calculated by Pearson correlation coefficients.	45
Figure IV-7. (a) Space- and time-resolved Raman spectra showing the evolution of isotope incorporation in LR regions in yeasts, different cells, (b) Percentage similarity among LR spectra at each time calculated by Pearson correlation coefficients. Each spectrum is an average of 25 different cells.	46
Figure IV-8. ¹³ C incorporation dynamics observed with incubation time in bulk experiments. (a) Amide I bands in PR spectrum at 1654 cm ⁻¹ (red) and 1620 cm ⁻¹ (blue) (b) Phenylalanine breathing mode in PR spectrum at 1003 cm ⁻¹ (red) and 967 cm ⁻¹ (blue) (c) ¹² C= ¹² C str at 1654 cm ⁻¹ (red) and ¹³ C-shifted 1602 at 1542 cm ⁻¹ (blue) from LR spectrum (d) 1602 cm ⁻¹ from LR spectrum	49
Figure IV-9. Time-lapse multimode Raman imaging of a single living <i>S.pombe</i> cell grown ¹³ C-glucose containing medium.	51

Figure IV-10. Time-lapse Raman imaging of other single living *S. pombe* cells grown in ¹³C-glucose containing medium.....55

List of Tables

Table III-1. Composition of LB-Miller medium20

Table III-2. Tentative assignments of Raman bands observed in planktonic *E.coli* spectrum .22

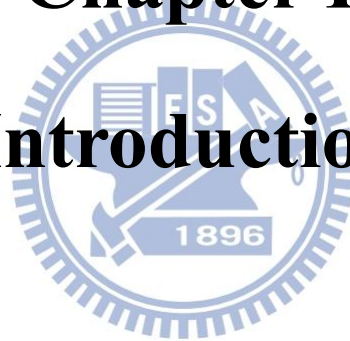
Table IV-1. Composition of Edinburgh Minimal Medium.....40

Table IV-2. Peak positions in ¹²C- and ¹³C-EMM, molecular component with their tentative assignments.....43



Chapter I

Introduction



Nature manifests its complexity through life. From time immemorial, people have been trying to understand nature's way of functioning, especially in relation to living things. But biology in the micro domain was kick started only after the discovery of microorganisms by Antony van Leeuwenhoek in 1676. Since then, it has been one of the major goals of researchers across various disciplines of science to understand the many complex phenomena occurring at the cellular level. Another major revolution in biology happened in 1953 when Watson and Crick discovered the structure of DNA [1], which led to much of the modern understanding of life at the molecular level. The wealth of knowledge accumulated in the last century has clearly revealed how dynamic living beings are, both at cellular and molecular level.

Hence it is very interesting and of primary importance to us, to investigate such complex biological processes happening in single cells as well as in larger biological communities such as biofilms. Many imaging techniques using optical microscope, confocal fluorescence microscope, scanning electron microscope, transmission electron microscope and atomic force microscope have been developed to probe the complexity in the structure of the cells. Though these techniques have the advantage of providing detailed structural images of cells, most of them either destroy or perturb the sample to a great extent. Especially in the case of fluorescence-based imaging methods, which are widely used by many biologists, there is always a need to introduce probe molecules/dyes to the target cell. Thus, it is not possible to explore unknown cellular components for which workable probes have not been developed yet. In other words, exploratory research is not possible. Moreover, there are reports which show that introducing probe molecules to a living cell often leads to unhealthy behaviors and may eventually alter its physiological conditions [2].

These microscopic approaches do not give any detailed information on the chemical composition of the sample, without which the investigation is incomplete. Another important

thing to keep in mind is that most of these methods usually can obtain information only in time- and space-averaged manner. In fact, quantitative understanding of the dynamic behavior of molecular composition and distribution in living systems still remains one of the challenging goals in biological sciences.

To advance our knowledge on how cells and other biological systems function in real time, it is desirable to investigate living systems in its own niche and as it is, either with minimal or ideally no perturbation. Raman spectroscopy does fulfill this demand; it offers a way to probe cellular biochemistry *in situ* and at the molecular level. Most importantly, it inherently bears much higher chemical specificity than any other imaging technique, as vibrational spectra are often referred to as ‘molecular fingerprints’. Needless to mention, Raman spectroscopy is label-free and the non-invasive and non-destructive characteristics of this technique allows for continuously monitoring of the dynamics in living subjects. In the present study, we utilize Raman micro-spectroscopy and imaging to gain fundamental and otherwise unobtainable biological information from both single cells and complex structures such as biofilms.

The remainder of this thesis consists of four chapters. Description of the experimental approach and data analysis methods used in this work is presented in Chapter II. Our Raman micro-spectrometer and imaging apparatus with an emphasis on its performance (spatial and axial resolution) is discussed first. Our laboratory-built confocal Raman micro-spectrometer has high sensitivity which enables us to measure Raman spectra of biological samples ranging from single living cells (*Schizosaccharomyces pombe*) to complex systems (*Escherichia coli* *biofilms*). The achieved lateral and axial resolutions of ~ 0.3 and ~ 2.5 μm , respectively, are sufficiently high to spatially resolve such samples. Multi-frequency Raman images can be obtained simultaneously in a single measurement. Next, a brief description is given on singular value decomposition analysis employed to reduce noise from data sets acquired with very low

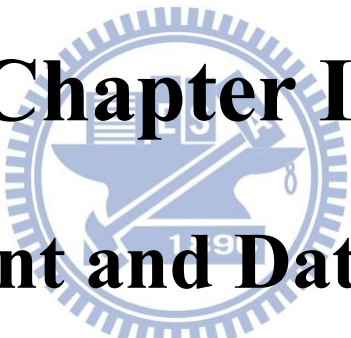
laser power and acquisition time.

Relatively large, complex biological samples will be the best to demonstrate the power of Raman micro-spectroscopy. Chapter III describes our studies on *Escherichia coli* (*E.coli*) biofilm. Molecular-level investigation of bacterial biofilms *in situ* is central to fully understand their important characteristics and related phenomena such as chronic human infections and quorum sensing. *E. coli* was chosen as the target of our study because it is a typical Gram-negative bacterium suited for a first step of systematic Raman studies. Raman spectra from a single planktonic *E.coli* and a model biofilm of *E.coli* grown for 30 hours under static condition were measured to gain information on distributions of biofilm constituents and physicochemical microenvironments. Certain microcolonies were identified in the biofilm where amino acid leucine was detected. Raman imaging measurements helped to visualize the distribution of leucine inside the colony in 3D. From this study, we eventually discovered high concentrations of leucine, forming leucine pools, in *E.coli* biofilms.

After successful studies on larger systems, we went on to study single cells, which are presented in Chapters IV. It is important to study processes that are otherwise not possible to investigate. One such important problem that has been much debated among biologists is the role of lipid droplets in cellular maintenance. We are particularly interested in the open questions as to whether lipid droplets are both spatiotemporally and functionally associated with proteins. To address this question, it is essential to be able to distinguish the biomolecular components that are actively synthesized from those that already exist. But ordinary Raman spectroscopy cannot do this job. Our strategy to circumvent this problem is to make use of stable carbon isotope (^{13}C) in combination with Raman spectroscopy. Results of the use of stable isotope labeled Raman micro-spectroscopy and imaging on fission yeast, *Schizosaccharomyces pombe* are presented in Chapter IV. Single cell time-resolved Raman

imaging experiments in fission yeast helped to visualize the intracellular distribution of both proteins and lipids, assimilation of ^{13}C and their dynamic reorganization within the cell. Strong co-localization of lipids and the actively synthesized proteins was observed, which proved that lipids indeed sequester proteins.



A faint, circular watermark of a university seal is centered behind the text. The seal features a central figure, possibly a lion or a similar heraldic animal, holding a staff or scepter. The year '1891' is visible at the bottom of the seal's inner circle. The outer ring of the seal contains text, which is mostly illegible due to the watermark's opacity.

Chapter II

Experiment and Data Analysis

II-1. Confocal Raman micro-spectrometer

All Raman measurements presented in this thesis, including space- and time-resolved measurements and imaging experiments, were performed using a laboratory-built confocal Raman microspectrometer [3], [4] and its schematic illustration is shown in **Figure II-1**. The 632.8-nm output of a He-Ne laser (Thorlabs) with a beam diameter of 0.98 mm was used as the Raman excitation source. Our scheme is similar to that of any contemporary Raman spectrometer. First, excitation laser light passed through a laser line filter to clean up any spontaneous emission. Then, in order to reduce the spot size at the focal point, the laser beam was magnified by a factor of ~ 2.7 using a lens pair to effectively cover the exit pupil of the objective. Collimation of the laser beam was also achieved in this step. The expanded beam was then introduced to an inverted microscope (Nikon) by a pair of an edge filter (Semrock; LP02-633RU-25) and a hot mirror (Thorlabs; FM02). The microscope was custom-made in collaboration with Nikon engineers by modifying a TE2000-U microscope. The beam was focused onto the sample by an oil-immersion objective (CFI Plan Fluor; 100 \times , NA = 1.3) placed on the microscope stage, and backward scattered light was collected by the same objective. The backward scattered light was guided along the opposite direction to the incoming path. Rayleigh and anti-stokes Raman scattered light was rejected at the edge filter and only Stokes Raman scattered light was transmitted. The Raman scattered light was then focused onto a 100- μm pinhole by a 150-mm lens and collimated by another 150-mm lens.

With this confocal configuration, a spatial resolution of about 0.3 μm in lateral direction and 2.7 μm in axial direction were achieved (see below). The Raman scattered light was dispersed by an imaging spectrometer (HORIBA Scientific; iHR320) and detected by a back-illuminated, deep-depletion, liquid-nitrogen cooled CCD detector (Princeton Instruments;

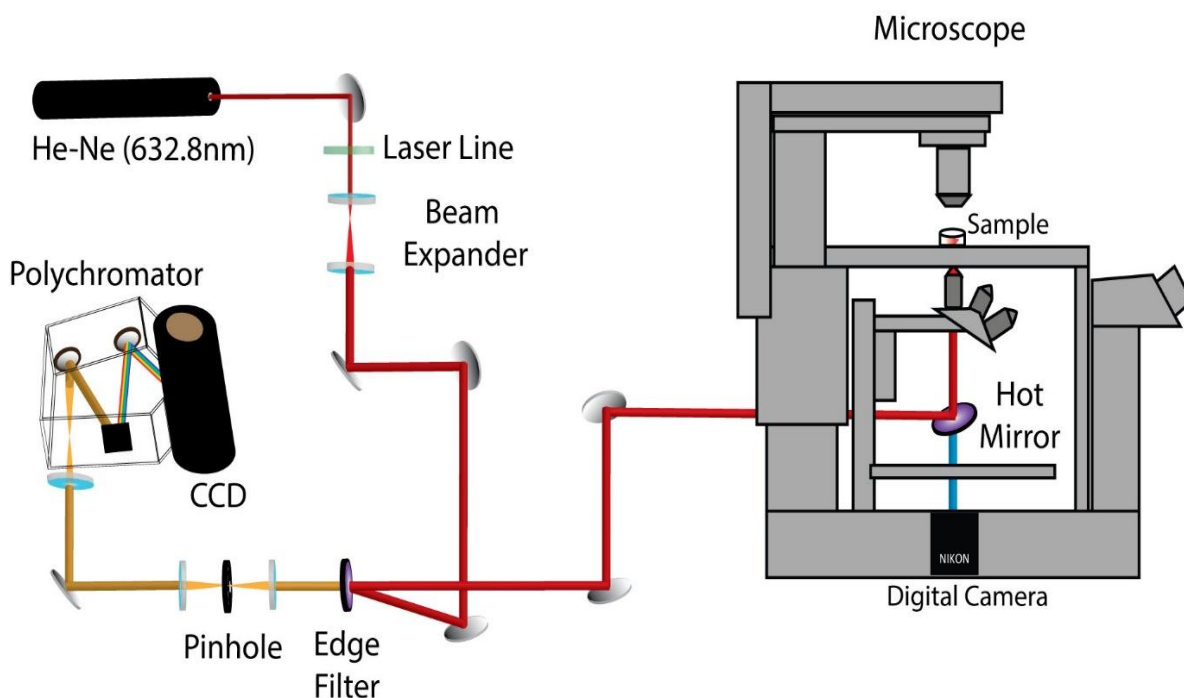


Figure II-1. Schematic representation of our laboratory-built confocal Raman micro-spectrometer.

Spec-10:100B) with 100×1340 pixels operating at -120 °C. A 600 grooves/mm grating was used. The resulting spectral resolution was 7 cm^{-1} , which was high enough in this work because the Raman spectra of biological samples usually exhibit relatively broad Raman bands. In addition, this grating can cover a wide spectral range over the fingerprint region (>2000 cm^{-1}). For bright-field observation, the sample was illuminated by a halogen lamp (or a mercury lamp) and optical micrographs were acquired by a digital camera (Nikon; DS-Ri1) mounted on a side port of the microscope.

For imaging experiments, the laboratory-built confocal Raman microspectrometer was also equipped with a high-precision piezoelectric nanopositioning stage (PI; P-563.3CD). A LabVIEW (National Instruments) program was run to automatically control the piezoelectric stage such that Raman imaging experiments were performed by translating the sample both horizontally and vertically. In the present work, the sample was translated with a 0.5 - μm step

in both X and Y directions. Because these steps were greater than the estimated lateral resolution (0.32 μm), they determined the effective spatial resolution in our experiments.

II-2. Estimation of lateral and axial resolutions

In order to evaluate the performance of our confocal Raman micro-spectrometer, it is crucial to know the resolution in both lateral (XY) and axial (Z) directions. First, to estimate lateral resolution, the intensity of the first-order phonon band of silicon at 520 cm^{-1} was measured while the laser spot was scanned horizontally, with 100 nm step size using the piezostage, through a sharp edge of a silicon wafer (a few μm inside the Si wafer through the edge until a few μm away from the wafer). The intensity of the silicon band will be strong when the laser hits inside the Si wafer, but as the laser spot approaches the edge, the intensity will drop rapidly and become negligible outside. Assuming that the edge of the Si wafer is infinitely sharp [i.e., described by a step function $H(x)$] and that the laser beam profile is a Gaussian function $g(x)$ with its full width at half-maximum (FWHM) being the lateral resolution, the measured intensity profile can be approximated by a convolution of $H(x)$ and $g(x)$. Here x is the scanned distance in X direction. By fitting the experimentally obtained intensity profile with **Equation II-1** [5], the lateral resolution can be estimated.

$$f(x, N, c, \sigma) = N \int_{-\infty}^{\infty} H(a')g(a' - x)da' = \frac{N}{2} \left(1 + \text{erf} \left(\frac{x - a}{\sqrt{2}\sigma} \right) \right) + c \quad (\text{II} - 1)$$

Here, N is a normalization constant, a is the onset of the step function, σ is the width of the Gaussian function, c is a constant, and erf denotes the error function. The lateral resolution is equal to $2\sqrt{2 \ln 2} \sigma$. Similarly, to estimate axial resolution, the intensity profile of a Raman band of cyclohexane at 801 cm^{-1} measured at a solvent glass interface was used. Raman intensity profiles as a function of the scanned distance in the X and Z directions are shown in

Figure II-2 (a) for lateral resolution and in **Figure II-2 (b)** for axial resolution, respectively.

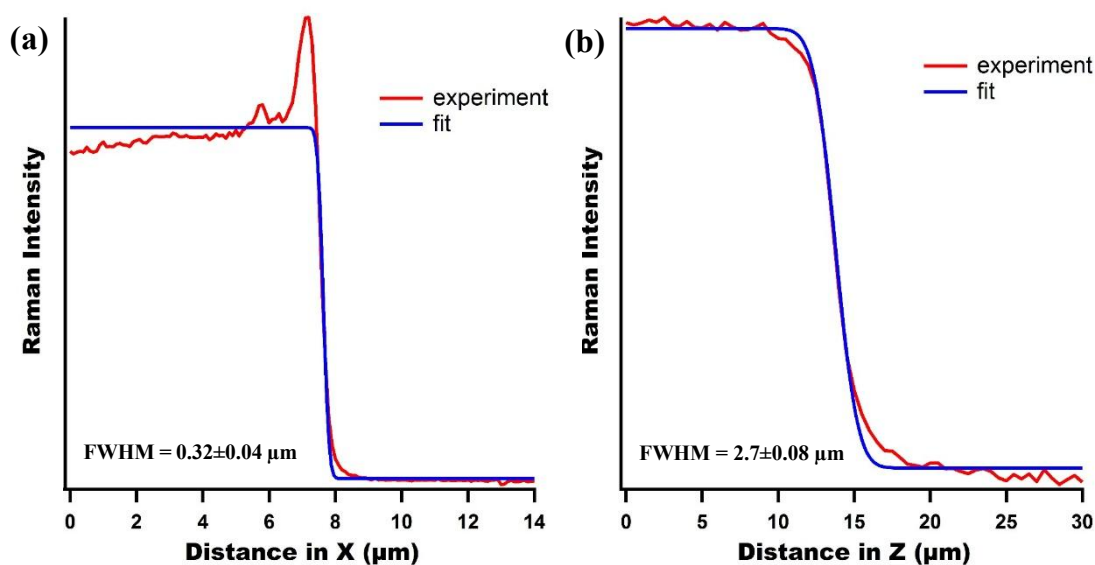


Figure II-2. Evaluation of (a) lateral and (b) axial resolution of our laboratory built confocal Raman micro-spectrometer. Observed Raman intensity in red and the best fit with the model function (**Equation II-1**) in blue.

The fitted results show that the lateral resolution is $0.32 (\pm 0.04) \mu\text{m}$ and axial resolution is $2.7 (\pm 0.1) \mu\text{m}$ in the axial direction. The errors here represent fitting precision.

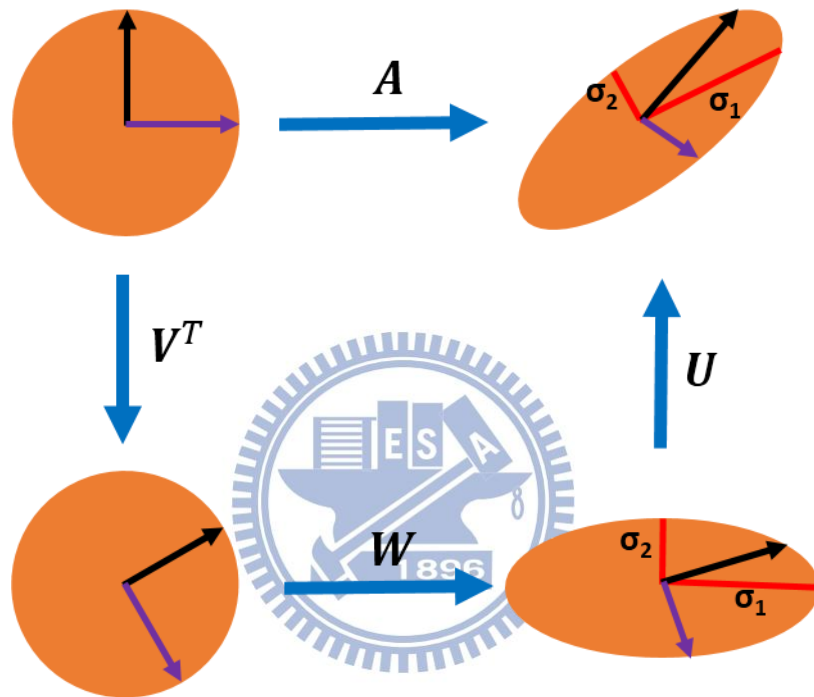
II-3. Singular value decomposition analysis

From our own experience and literature [6], we understand that cell viability decreases with increasing excitation laser power and exposure time. Since we want to see the dynamics in single cells and other biological samples that often take long time (e.g., days or even longer), it is very important not to disturb the regular functioning of the cell. So, in order to provide a better growing environment for the cells, we need to use sufficiently low laser power (1 mW) with short exposure time (typically 1 to 2 s). But the resulting disadvantage is that the Raman signal will be reduced drastically under such low experimental conditions, resulting in poor signal-to-noise (S/N) ratio spectra and low Raman image quality.

To circumvent this practical problem, we make use of a numerical post-treatment

method based on singular value decomposition (SVD). This approach has been used successfully by us [3], [4], [7] and several other researchers [8]-[10] as a spectral de-noising technique.

SVD is a mathematical technique that factorizes an arbitrary $m \times n$ matrix A into the product of three matrices as $A = UWV^T$. Geometrically, SVD decomposes A into three simple



$$A = UWV^T$$

Figure II-3. Principle of SVD. The upper left shows the unit disc together with the two canonical unit vectors. The upper right shows the action of A on the unit disc: it distorts the circle to an ellipse. The SVD decomposes A into three simple transformations: a rotation V^T , a scaling W along the coordinate axes and a second rotation U . The SVD gives σ_1 and σ_2 which are just the singular values that occur as diagonal elements of the scaling W .

transformations: a rotation V^T , a scaling W along the rotated coordinate axes and a second rotation U as shown in **Figure II-3**. The SVD reveals the lengths σ_1 and σ_2 of the semi-major and semi-minor axes of the ellipse which are just the singular values that occur as diagonal elements of the scaling W . The rotation of the ellipse with respect to the coordinate axes is given by U .

Mathematically, U is an $m \times n$ column-orthonormal matrix (also called left singular values), W an $n \times n$ diagonal matrix of positive singular values, and V an $n \times n$ orthonormal

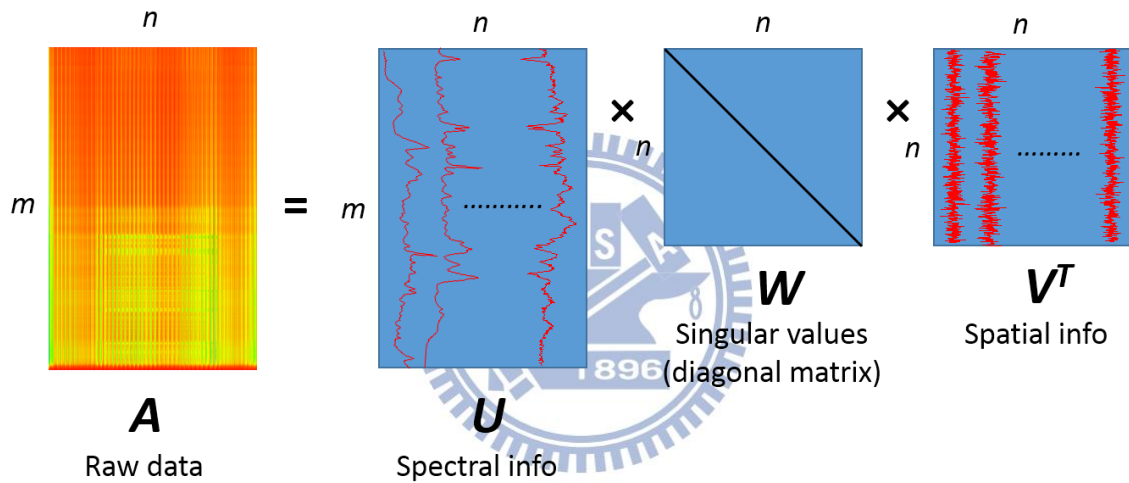


Figure II-4. Graphical representation of SVD. Raw data matrix A can be factorized into a product of three matrices U (contains spectral information), W (contains singular values) and V^T (spatial information of each spectral component)

matrix (right singular matrix). U and V represent the spectral and positional matrices, respectively as shown in **Figure II-4**. Only components of U and V having significantly large singular values were retained to reproduce matrix A , because other components with much smaller singular values contributed to the original data negligibly and can be regarded as noises. The matrix A was then reconstructed by using the components of U and V associated with large singular values. The number of singular values retained in this reconstruction was typically in

between 10-15. The main criterion for determining how many components are taken into account was whether or not the spectral component of \mathbf{U} corresponding to a particular singular value shows definite Raman features. The SVD was computed in Igor Pro (WaveMetrics) using LAPACK routines. **Figure II-5** illustrates how well SVD denoising works. Space-resolved Raman spectra of a fission yeast cell are compared before and after the SVD. It is clear that the SVD reduces noises dramatically. As compared in **Figure II-5 (b) and (c)**, the Raman image constructed for the 1602 cm^{-1} band from the raw data (without SVD) is featureless due to noisy spectra, but the image constructed from the SVD-analyzed data shows high contrast.



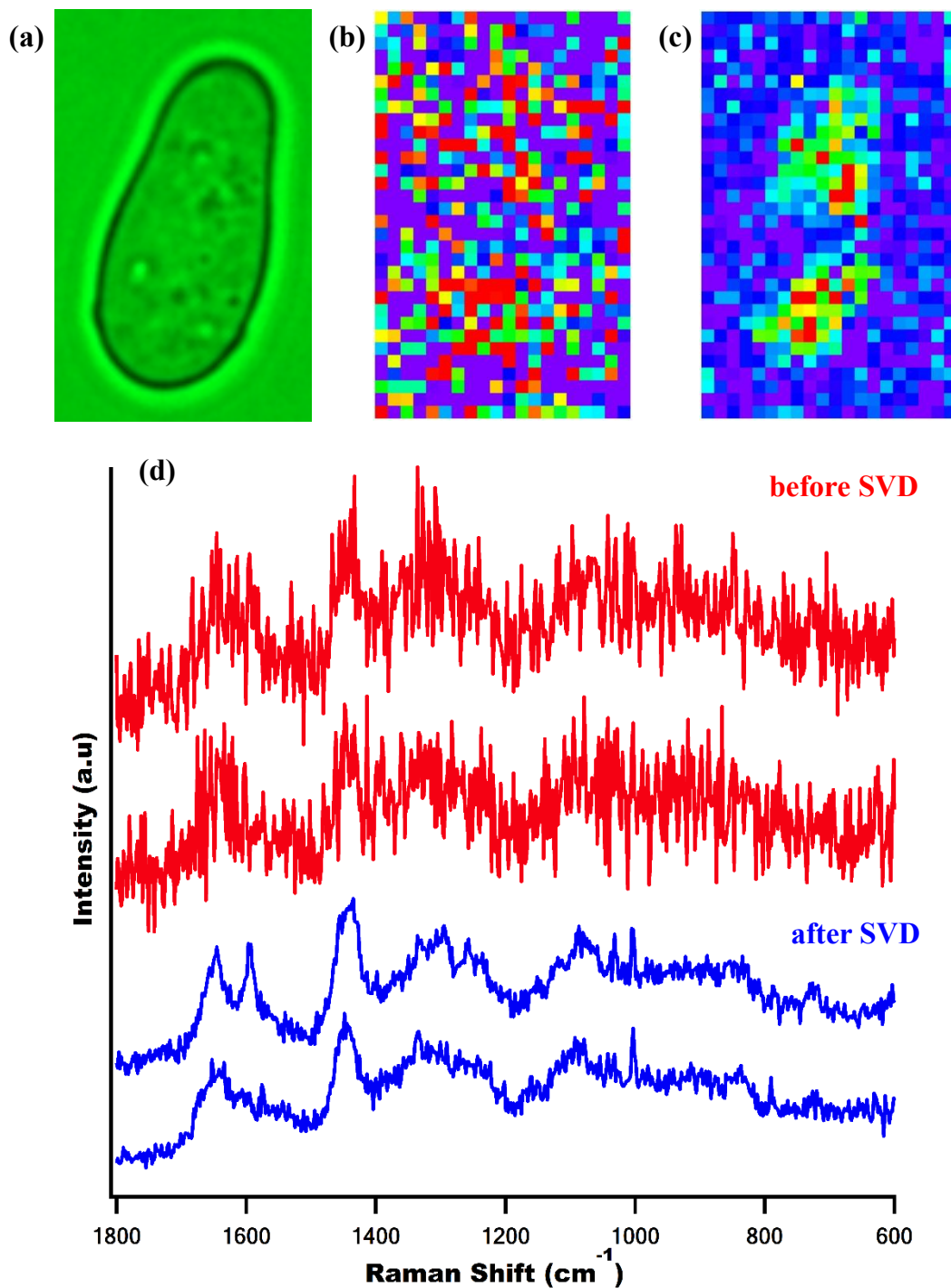
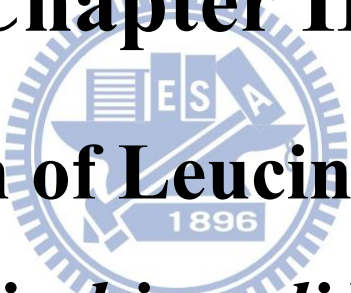


Figure II-5. (a) Optical image of a typical fission yeast cell; (b,c) Raman images constructed for 1602 cm⁻¹ with raw data before SVD (b) and after SVD analysis (c); and (d) representative space-resolved Raman spectra from the same data which were acquired with an exposure time of 1.5 s and 1 mW laser power. The SVD-treated spectra (blue) exhibit much higher S/N than the corresponding raw data

Chapter III

Detection of Leucine Pools in

***Escherichia coli* Biofilm**

The logo of the University of South Florida is centered behind the text. It is a circular seal with a gear-like outer edge. Inside the seal, there is a stylized sun or starburst at the top, a book in the middle, and the year '1896' at the bottom. The letters 'E', 'S', and 'F' are arranged around the central elements.

III-1. Introduction

Ever since Anton Van Leeuwenhoek reported the discovery of microorganisms in 1676, they have been characterized primarily as planktonic, freely floating cells. Following the discovery, their growth characteristics were studied extensively in nutritionally rich culture media to describe them. Undoubtedly, these studies have been highly informative and have advanced our knowledge on the biology of bacteria. However, in the last four decades, the discovery of many microbiological phenomena that surface-associated microbes exhibit distinct phenotypes from that of their planktonic counterparts aroused significant attention among the scientific community to understand the microbial life in the naturally occurring forms known as biofilms.

There were some observations as early as 1940 that introducing a surface enhances bacterial growth and activity, but the first detailed study of biofilm was reported by Jones et.al. in 1969 [11]. They found that biofilms contain a variety of microorganisms by examining biofilms on trickling filters in a wastewater treatment plant by electron microscopy. Additionally they also confirmed for the first time that the extracellular matrix was mostly composed of polysaccharides. Later in 1973, studies on microbial slimes from industrial water systems by Characklis showed that biofilms are resistant to disinfectants such as chlorine and are tightly bound to the surface [12]. In 1978, from the studies on microorganisms in dental plaque and attached communities in mountain streams, Costerton et.al. proposed that microbes adherent to the living or non-living surfaces gain special characters depending on the environmental conditions [13]. Since then biofilms became a topic of interest among researchers across various disciplines.

III-2. What are biofilms?

Bacteria in nature usually live most of their life as members of a ‘socialized’ community called a biofilm rather than as free-living cells. A biofilm is a structured consortium of sessile bacterial cells irreversibly associated on a biotic or an abiotic surface. In a biofilm, cells are encased in a matrix of self-secreted extracellular polymeric substances (EPS) primarily composed of polysaccharides along with proteins and DNA. Although traditional microbiology has focused on planktonic bacteria, it is bacterial cells adopting the biofilm lifestyle that play an essential role in various processes such as bacterial infections [14], [15], wastewater treatment [16], and bioremediation [17]. Indeed, a public announcement by the US National Institutes of Health reads “Biofilms are medically important, accounting for over 80% of microbial infections in the body”.

Biofilm bacteria are known to show exceedingly high resistance to antimicrobial agents. Furthermore some bacterial species in their biofilm mode of growth can communicate with one another via chemical signalling in the way that the cell density inside microcolonies (cell clusters) in the biofilm regulates cell’s transcriptional processes (quorum sensing). It has been shown that hormone-like signalling molecules termed autoinducers are responsible for gene regulation and resultant biofilm formation. In fact, bacterial biofilms can function as if they were tissues of a higher organism. In all these processes, various biomolecules serve as chemical signals, regulators, and structural components [18]. For example, in many species including *Pseudomonas aeruginosa* [19], [20] and *Staphylococcus aureus* [21], extracellular DNA has been shown to be required for initial biofilm formation.

Recently it has been reported that some D-amino acids trigger biofilm disassembly in *Bacillus subtilis* and other bacteria [22]. All those characteristics, which make bacterial cells in the biofilm milieu unique and quite different from their planktonic counterparts, are closely

associated with the structure of biofilms and molecular distributions therein.

III-3. Developmental stages in biofilms

Biofilm development is a complex process involving several stages, each with unique characteristics. It can be divided into five stages [23], [24] (**Figure III-1**).

1. Initial attachment: reversible attachment of cells to the surface
2. Irreversible attachment: production of EPS, resulting in more firmly adhered irreversible attachment of cells
3. Maturation I: early development of biofilm architecture in which active recruitment of cells from the bulk fluid takes place, and formation of microcolonies
4. Maturation II: steady increase in size, which leads to formation of mature cell clusters
5. Dispersion: dispersal of cells from mature colonies to form new microcolonies

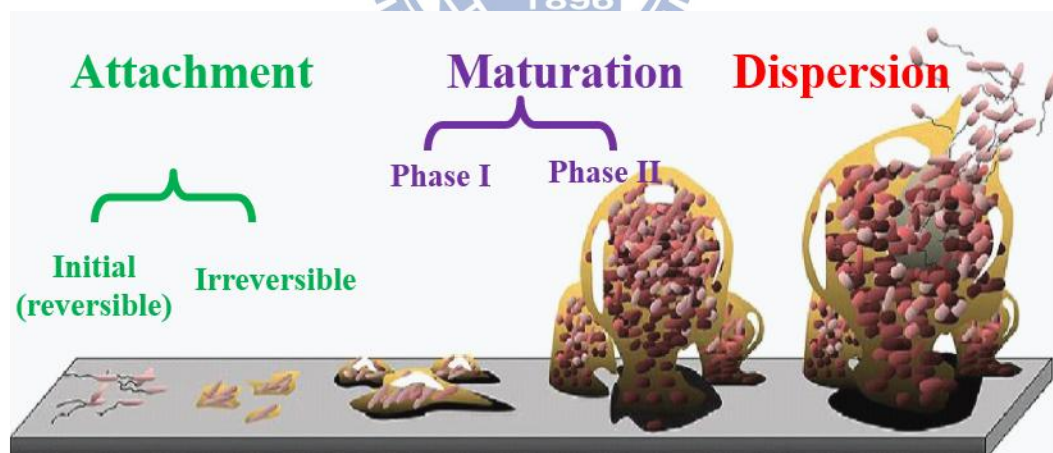


Figure III-1. Developmental stages of a biofilm

Source: Monroe D. Looking for Chinks in the Armor of Bacterial Biofilms.

III-4. General methods to study biofilms

In the early days, most of the research on biofilms relied on techniques such as electron microscopy and standard biological characterization protocols. Later, to understand the biofilm architecture and distributions of biofilm constituents in a non-destructive manner, a variety of optical microscopic methods have been developed and applied. Most commonly used technique for biofilm studies is confocal laser scanning microscopy (CLSM). This method is based on detecting fluorescence from a dye probe introduced to the sample, allowing for three-dimensional (3D) *in situ* visualization of the biofilm structure with high sensitivity and sub- μm resolution. CLSM studies have revealed that, despite the name of biofilm, the biofilm structure is far more complicated than what one would imagine from a film: a biofilm often consists of microcolonies and channels through which water and other fluids can flow [25]. In CLSM, however, staining cells in a biofilm with an appropriate fluorescence dye is a prerequisite for imaging. Thus, as yet unknown substances can never be explored by this method, because relevant fluorescent probes for the target are not known as well. CLSM (fluorescence imaging) can provide space-resolved information that the conventional biochemical assays often lacks, but it has only limited access to the information on molecular structures and microenvironments in biofilms.

As a first step to fully understand how the biomolecules in biofilms, regardless of whether they are already identified or not, fulfill their advanced functions, we use a label-free Raman imaging method to study the constituents of an *Escherichia coli* (*E.coli*) biofilm *in situ* and to visualize their distributions in the biofilm.

III-5. Escherichia coli

E. coli was the bacterium of choice for our demonstration, a typical bacterium suited for a first step of systematic Raman studies, since it is the most widely studied prokaryotic model organism. It is a gram-negative, facultative anaerobic, rod shaped bacterium. Most of the strains

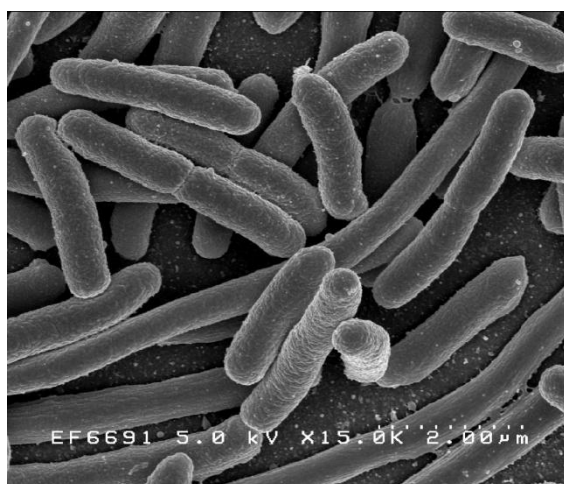


Figure III-2. Scanning electron micrograph of *E.coli* grown in culture medium and adhered to a cover slip

Source: Rocky Mountain Laboratories, NIAID, NIH

are harmless and are part of normal flora of the gut preventing the establishment of pathogenic bacteria within the intestine. Typically they are 2 μm in length and 0.5 μm in diameter as can be seen from **Figure III-2**.

III-6. Raman spectrum of a single planktonic *E. coli*

A laboratory strain of *E.coli* (XL1-blue) was routinely cultured in LB-Miller medium

Table III-1. Composition of LB-Miller medium

S.No	Component	Weight (g/L)
1	Tryptone	10
2	Yeast extract	5
3	NaCl	10

at 37 °C, whose composition is given in **Table III-1**. As a preliminary step, the Raman spectrum of a single planktonic *E. coli* was measured by laser trapping (632.8 nm for both trapping and excitation) with a minimal laser power of 3 mW at the sample point. The planktonic Raman

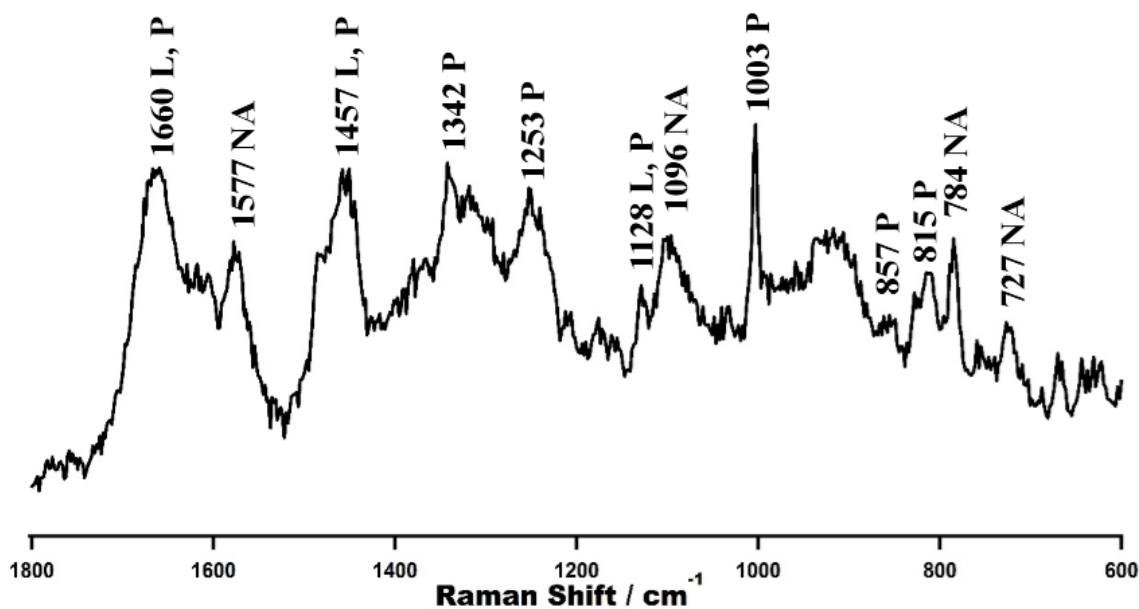


Figure III-3. Typical Raman spectrum of a single *E. coli* bacterium, with 632.8 nm excitation, optically trapped at the focal point. Raman bands characteristic of proteins P, lipids L and nucleic acids NA are observed. (Laser power, 3 mW; exposure, 100s)

spectrum (**Figure III-3**) shows several bands characteristic of lipids, proteins and nucleic acids. Main features are the amide I (mainly C=O stretch of amide bonds) band at 1660 cm⁻¹, the CH bending of the aliphatic chain at 1342 and 1457 cm⁻¹, and the breathing mode of the phenylalanine residue at 1004 cm⁻¹. Nucleic acid bands at 784 and 1096 cm⁻¹ attributable to the (deoxy) ribose-linked phosphodiester backbone vibrations of RNA (DNA) were observed. Cytosine could contribute to the 784 cm⁻¹ band as well. The doublet observed at 815 and 857 cm⁻¹ is known as the tyrosine doublet arising from the Fermi resonance of a ring-breathing vibration and the overtone of an out-of-plane ring-bending vibration of tyrosyl residues [26]. The bands at 670 and 725 cm⁻¹ are due to nucleobases guanine and adenine, respectively. The assignments [27]-[30] are summarized in **Table III-2**.

Table III-2. Tentative assignments of Raman bands observed in planktonic *E.coli* spectrum

Peak Position (cm ⁻¹)	Assignment		
	Protein	Lipid	Nucleic Acid
1660	Amide I	C=C str	
1577			A, G ring str
1457	$\delta(\text{CH}_2)$ scis CH ₂ def	$\delta(\text{CH}_2)$ scis CH ₂ def	
1342	$\delta(\text{CH})$		
1253	Amide III		
1128	C-N, C-C str	C-C str	
1096			PO ₂ ⁻ sym str
1003	Phenylalanine		
857	Tyrosine		
815	Tyrosine		
784			C, T
727			A

III-7. Space-resolved Raman spectra of *E. coli* biofilms

E. coli biofilms were grown on a glass-bottomed dish at 37 °C under static conditions for 30 hours. The static condition here meant that, in the biofilm growth and subsequent Raman measurements, we did not employ any continuous-flow system in which the biofilm would always be subject to hydrodynamic shear force. Since *E. coli* biofilms are generally known to be fragile, we did not wash the biofilm sample. Instead, to remove the planktonic population and suppress fluorescence, we gently pipetted excess LB medium out from the edges of the dish. Neither cell staining nor immersing the biofilm in a suspension of metal nanoparticles [31], [32] to enhance Raman signals was required. Thus, our method can be said to look at the target with minimum external perturbation.

The sample was then transferred directly to the microscope stage for Raman measurements without any further pre-treatment. To obtain space-resolved Raman spectra of the 30-hour old *E. coli* biofilm, we fixed the focal plane of the excitation laser beam at approximately 3 μm above the substrate and collected Raman scattered light from selected locations inside/outside the microcolony on the plane. To avoid possible photo bleaching and heat accumulation, we used laser power of 3 mW at the sample point throughout the present study. For reference, the Raman spectrum of a planktonic *E. coli* cell was also measured using optical trapping. A 60 s exposure time for the Raman spectra of the biofilm and 100 s for that of the planktonic cell were used.

Almost everywhere in the unwashed *E. coli* biofilm, a number of microcolonies were found as shown in **Figure III-4**. Their sizes were diverse, ranging from $\sim 5 \mu\text{m}$ to several tens

of micrometers wide. The morphology varied as well from one microcolony to another. **Figure III-5 (a)** shows one of the colonies on which further measurements were done, while **Figure III-5 (b)–(d)** compares the space-resolved Raman spectra, for the spectral range 400–1800 cm^{-1} , recorded inside and outside the microcolony at $\sim 3 \mu\text{m}$ above the substrate with that of a planktonic *E. coli* cell measured independently using optical trapping. The extracolony spectrum was almost identical to the planktonic Raman spectrum with few exceptions including the Raman band at 1408 cm^{-1} . This band is due probably to the COO^- symmetric stretch of polysaccharides such as alginates which are a major constituent of the extracellular matrix[25], [31].



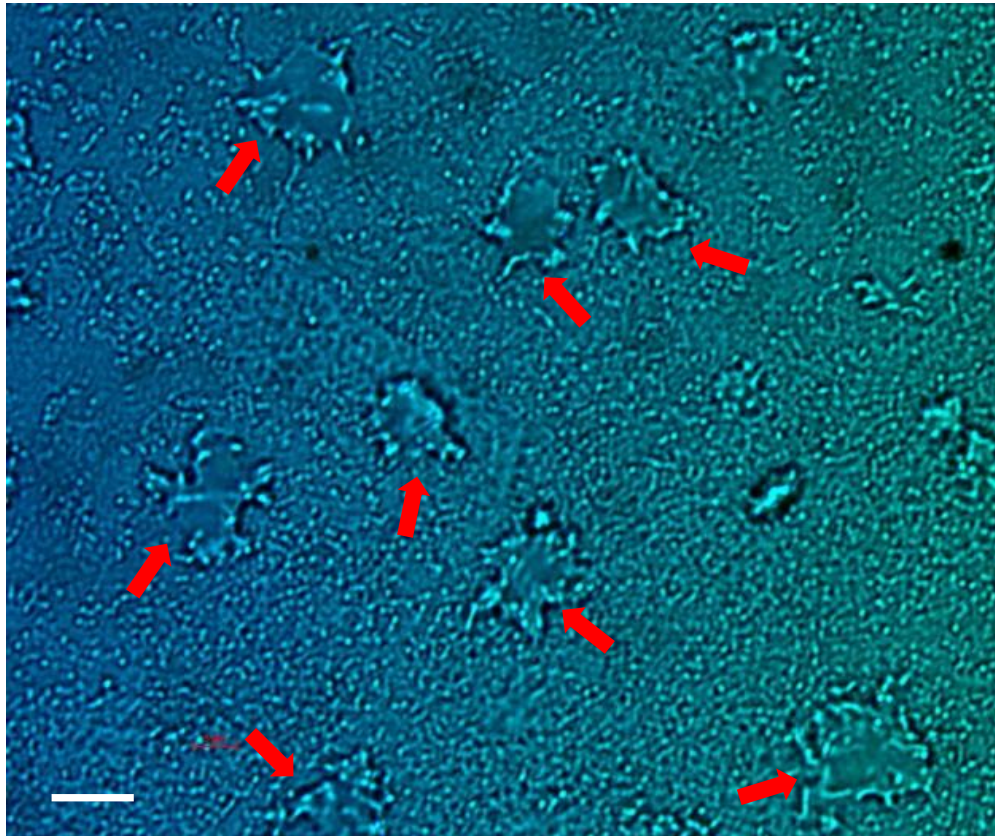


Figure III-4. Optical micrograph of a 30-hour old biofilm.

Red arrows indicate microcolonies formed in the biofilm.

Scale bar = 10 μm .

The extracolnial and planktonic spectra represent a typical cellular Raman spectrum dominated by proteins and DNA/RNA bands. These results, along with the optical micrograph [Figure III-5. (a)], show that the intercolonial space of the biofilm was filled with a dense population of *E. coli* cells held together by the extracellular matrix.

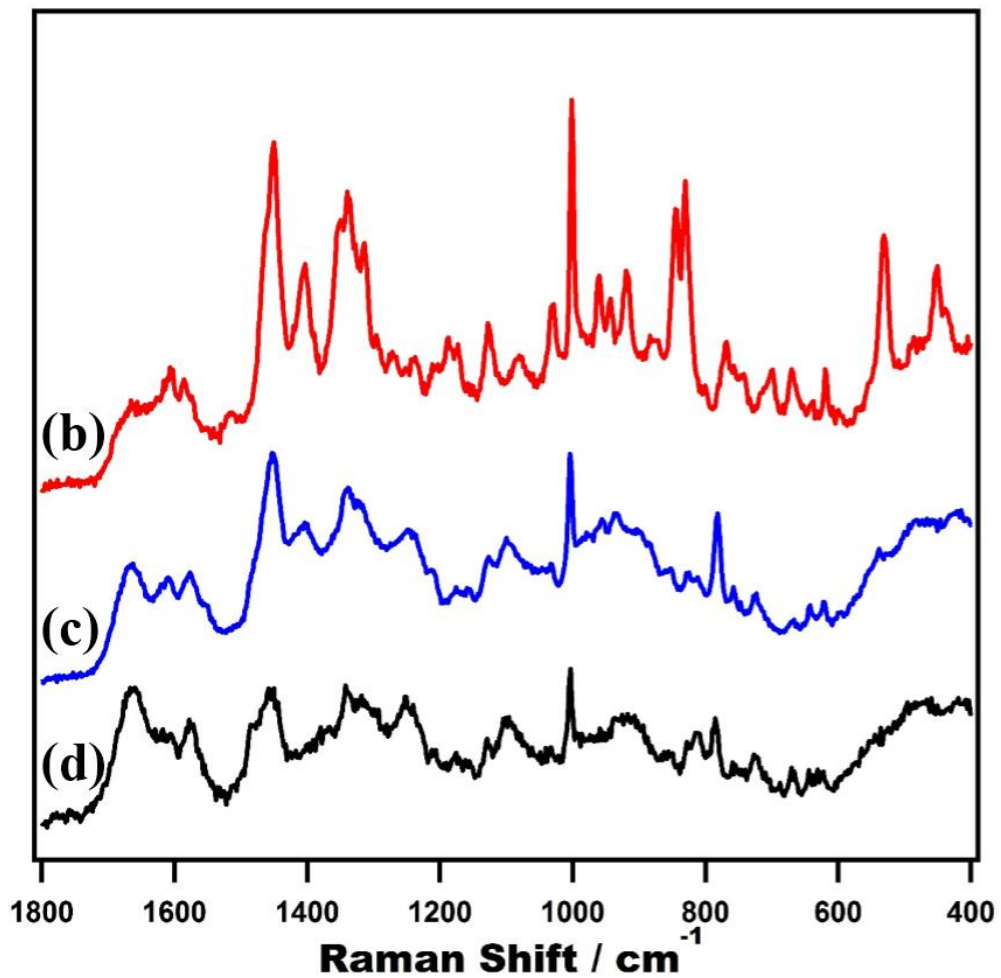
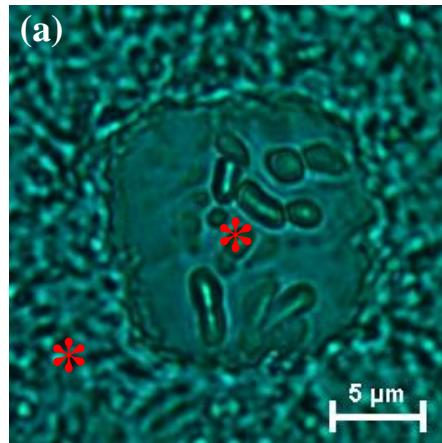


Figure III-5. (a) Optical micrograph of a single microcolony in 30 h old biofilm on which further experiments were done. Space-resolved Raman spectra of the 30-h old *E. coli* biofilm (b) intracolony, (c) extracolony and (d) a planktonic *E. coli* cell. Stars denote the positions at which (b) and (c) are recorded.

The intracolony spectrum differs substantially from the extracolony spectrum, indicating distinct chemical composition of the microcolony. By scrutinizing Raman spectra of biomolecules that could potentially occur in the microcolony, we found that the intracolony Raman spectrum resembles both in peak positions and in spectral pattern remarkably well to that of crystalline L-leucine [Figure III-6 (b)]. We also considered other amino acids such as L-isoleucine and L-valine that are close in chemical structure to L-leucine as possible candidates, but the overall agreement of spectra was not satisfactory at all [Figure III-6 (c),(d)].

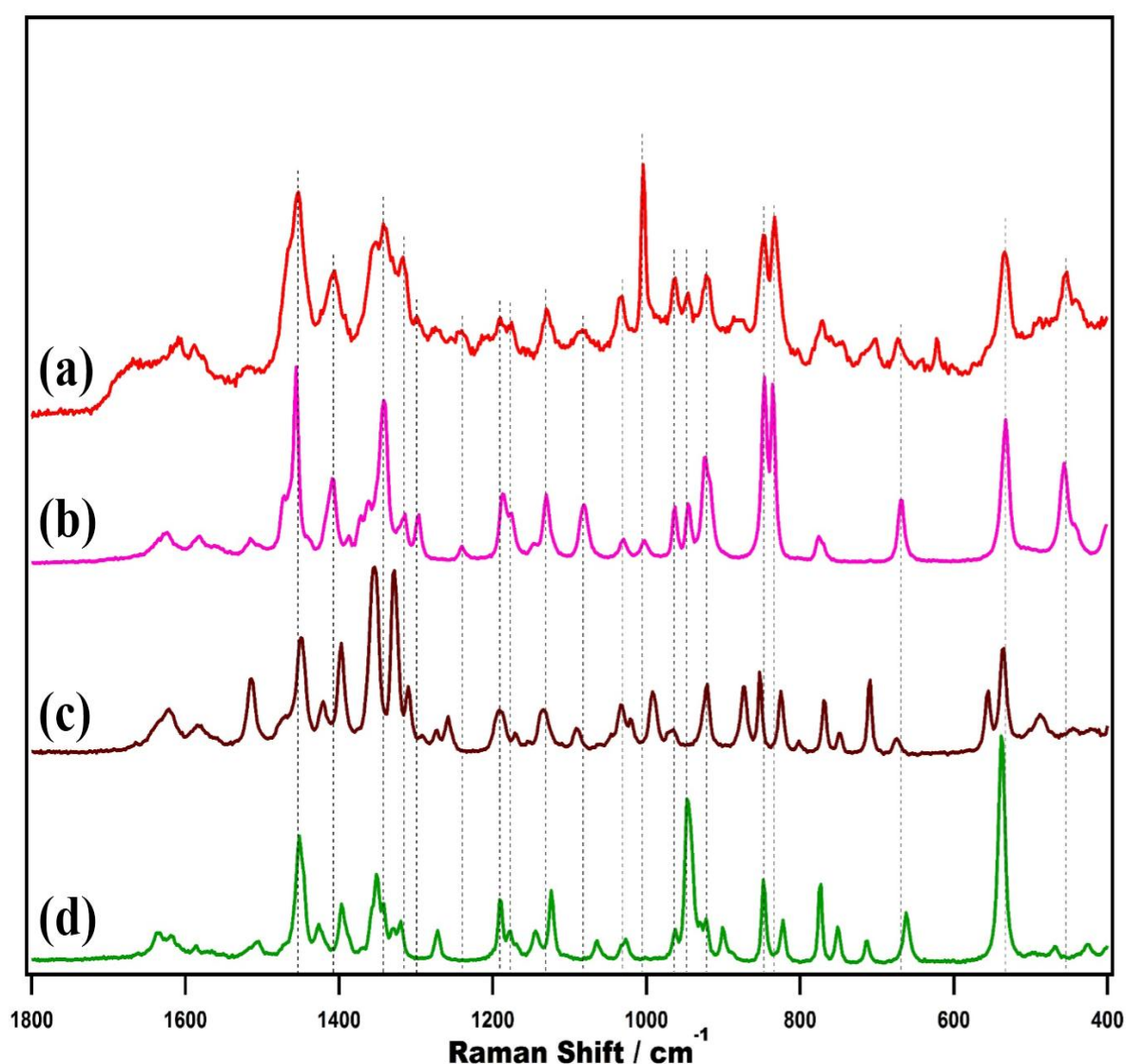


Figure III-6. Comparison of (a) intracolony Raman spectrum with those of crystalline (b) L-leucine, (c) L-isoleucine and (d) L-valine

Thus, we conclude that there were high concentrations of leucine (possibly with a minor contribution from phenylalanine) within the *E. coli* biofilm microcolony, forming a leucine pool.

III-8. Raman imaging of a single microcolony

After understanding the molecular origin of the intracolony Raman spectrum, it is essential to visualize its distribution in the colony, for which we performed Raman imaging measurements. To scan the laser spot across the biofilm, an XYZ piezoelectric translation stage was installed in our microscope. Since the axial resolution was much poorer than the lateral resolution, we translated the biofilm with a 0.5 μm step in the XY direction and a 1 μm step in the Z direction. In the present case, the scanned region containing the microcolony measures $25 \times 25 \mu\text{m}^2$. At each pixel, the Raman spectrum was recorded with a 1 s exposure time and denoising was performed using SVD as mentioned Chapter II. Then multi-frequency Raman images were constructed simultaneously for virtually all the Raman bands involved in the spectra. Since Raman intensities are proportional to molecular concentrations, those images directly visualize molecular distributions in a section of the 30-hour old *E. coli* biofilm.

Figure III-7 displays eight representative Raman images, which directly visualize the distributions of the biofilm constituents. Two images at the Raman shift of 1097 and 782 cm^{-1} representative of DNA and six images at 1408, 1130, 922, 847, 671 and 533 cm^{-1} representative of amino acid leucine are displayed together with the optical micrograph of the scanned region. As expected from the space-resolved Raman data, Raman images of DNA show the yellow (medium to high intensity) pattern outside the microcolony, while those constructed for the bands observed in the intracolony spectrum manifest distributions localized inside the structure.

Although the distribution patterns within the microcolony are highly heterogeneous, they appear to be virtually the same for all the Raman bands **Figure III-7 (d)-(i)**. This strongly supports the idea that the microcolony was composed essentially of a single molecular species, namely, leucine. Otherwise, Raman images would vary largely depending on Raman bands.

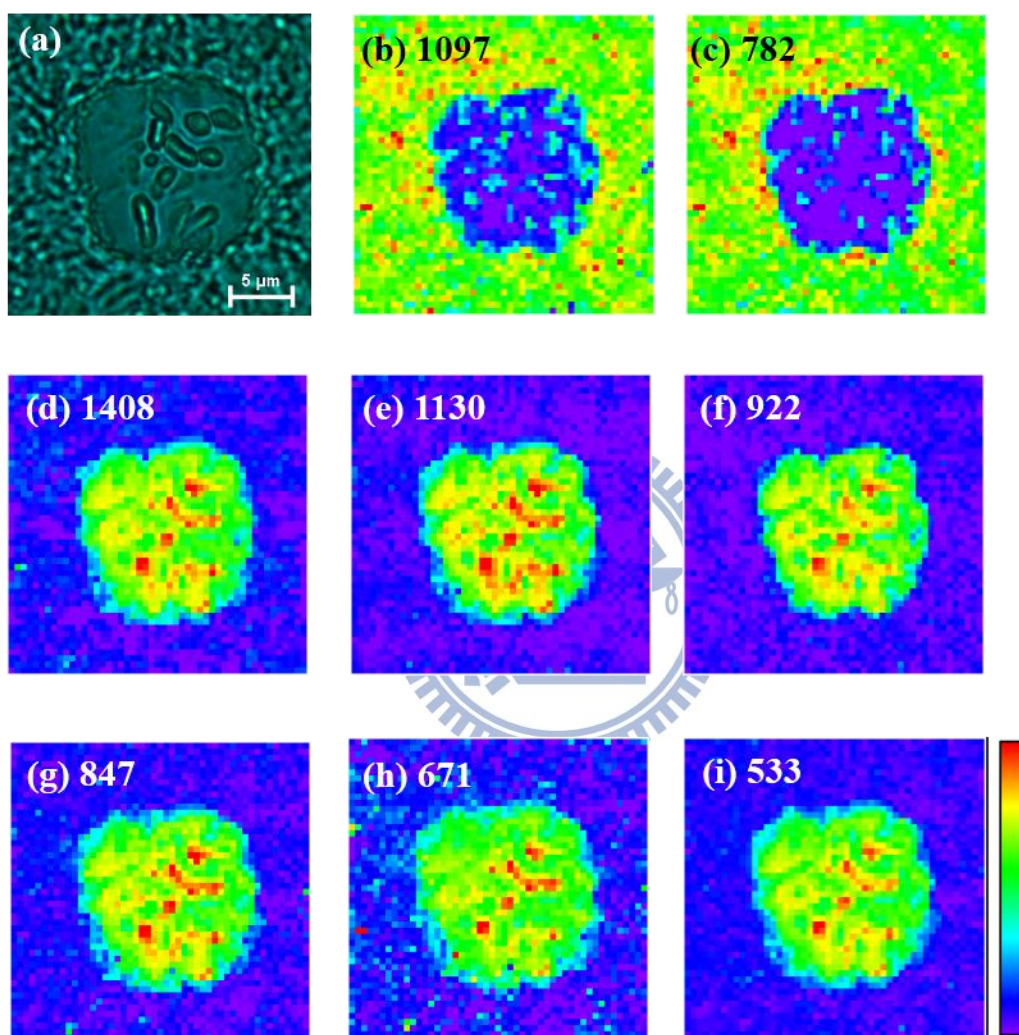


Figure III-7. (a) Optical micrograph of the scanned region and Raman images of the 30-h-old *E. coli* biofilm of the Raman bands at (b) 1097, (c) 782, (d) 1408, (e) 1130, (f) 922, (g) 847, (h) 671, and (i) 533 cm^{-1} . Images (b) and (c) represent the DNA distribution, while images (d)–(i) represent the leucine distribution.

Different color scale applies to each image. Scale bar = 5 μm .

III-9. Three dimensional (3D) Raman imaging

Once we completed a two-dimensional (XY) scan at $Z = 3 \mu\text{m}$, we translated the *E. coli* biofilm along the Z axis from $Z = 0\text{--}6 \mu\text{m}$ at $1 \mu\text{m}$ intervals and obtained Z-stacks of Raman images, as displayed in **Figure III-8**. In this way we realized full 3D, chemical visualization of the *E. coli* biofilm without resorting to cell staining. Although the Z scan is less informative with respect to biofilm heterogeneity because of a $2 \mu\text{m}$ axial resolution, we were able to estimate the height of this particular microcolony to be $4\text{--}5 \mu\text{m}$. Scanning in the Z direction would be more meaningful for thicker ($>10 \mu\text{m}$) biofilms.

Raman sectioning results are also consistent with the idea of a single species (leucine) being present in the microcolony as even the 3D Raman images constructed for several bands corresponding to leucine [**Figure III-8 (b),(c)**] show a similar pattern.

III-10. Why leucine?

The most important question to ask in this study is the biological role of leucine accumulation in the biofilm. Some clues to address this question can be found in the literature. Valle et al. found that *E. coli* biofilms secreted valine under continuous-flow conditions [33]. In contrast to their study, our *E. coli* biofilm was grown under static conditions, giving rise to both hydrodynamically and nutritionally distinct environments for the biofilm. Given the well-known phenomena of microbial growth inhibition and its antagonism caused by amino acids [34], [35], it is plausible that our *E. coli* biofilm may have used the localization of leucine to adapt to the static environment during its early stage development. This interpretation is only speculative and more experiments (both spectroscopic and biochemical) will surely be required to clarify the biological significance of our unique finding.

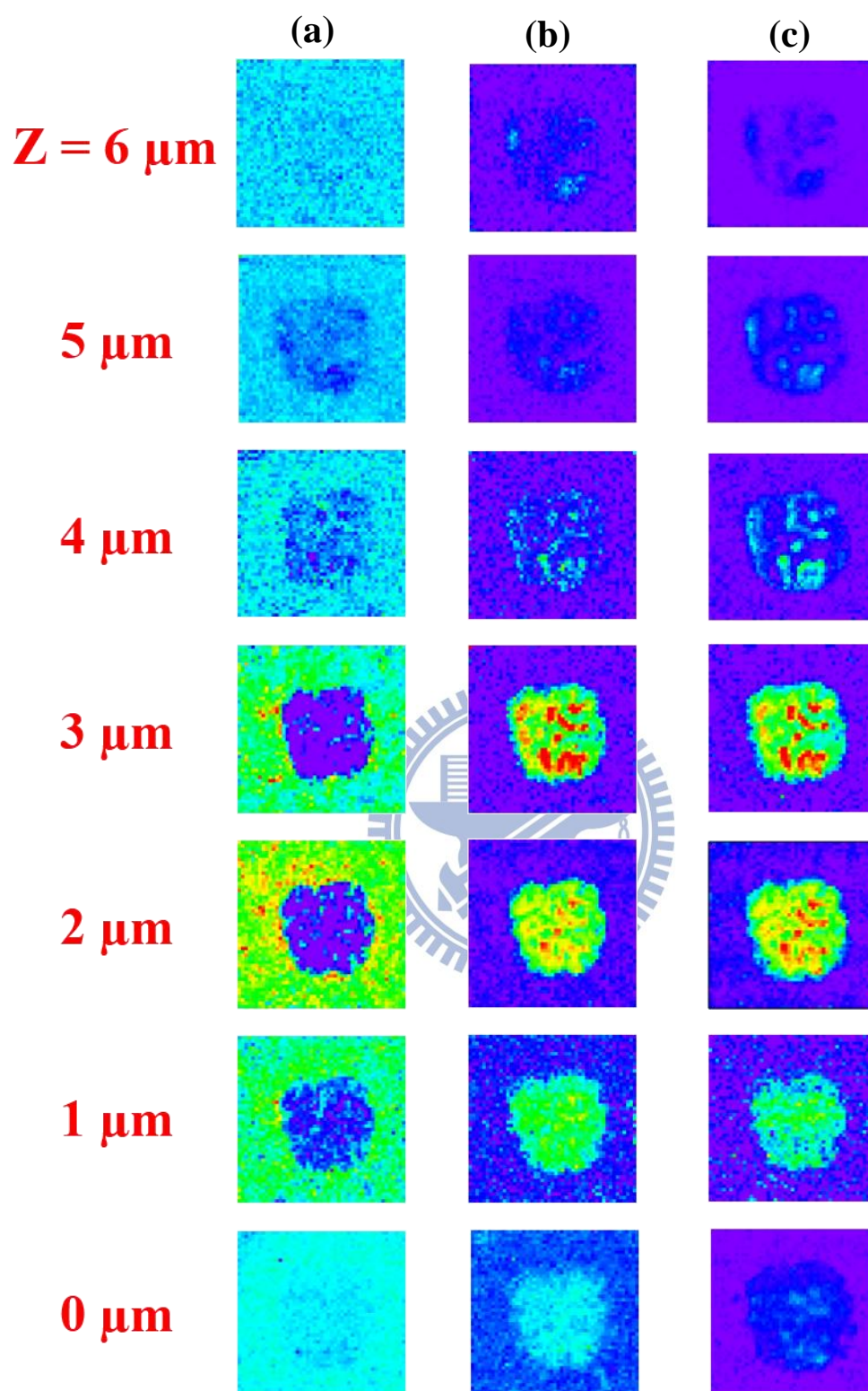


Figure III-8. Raman sectioning of the 30-hour-old *E. coli* biofilm Z stacks of the Raman images at (a) 782 cm^{-1} (the O–P–O symmetric stretch plus contributions of cytosine and thymine vibrational modes), (b) 922 , and (c) 1408 cm^{-1} .

III-11. Conclusion

In summary, we have discovered leucine pools in a nascent *E. coli* biofilm by using Raman imaging, where high levels of leucine were accumulated. We have also demonstrated that Raman imaging is a powerful tool for detecting *in situ* and identifying key biomolecules involved in biofilms even if they are yet unknown (i.e., possibility of exploratory research). We hope this study will open up new avenues for developing a simple but effective chemical means that will enable molecular-level elucidation of bacterial biofilms.



Chapter IV

Visualization of Dynamic Proteome Localization to Lipid Droplets in Single Fission Yeast Cells Using Stable Isotope Probing

IV-1. Introduction

Lipid droplets (LDs), also called lipid bodies or fat bodies, are globular organelles that are ubiquitously found in most eukaryotic cells from yeast to mammals. LDs are cytoplasmic structures which store neutral lipids in its core. Unlike other intra cellular organelles (aqueous compartments separated by lipid bilayers), LDs have a unique physical structure. LDs' core is surrounded by a single layer of phospholipids (polar) with some embedded proteins, separating it from the aqueous cytoplasmic space. The core is primarily constituted by triacylglycerols (TAG) and steryl esters (SE), crucial substances for cells (**Figure IV-1**). These molecules cannot serve as direct building blocks for lipid bilayers as they lack charged groups. Instead, upon requirement, these can be hydrolysed to sterols, diacylglycerol and fatty acid which can mainly be used to derive energy.

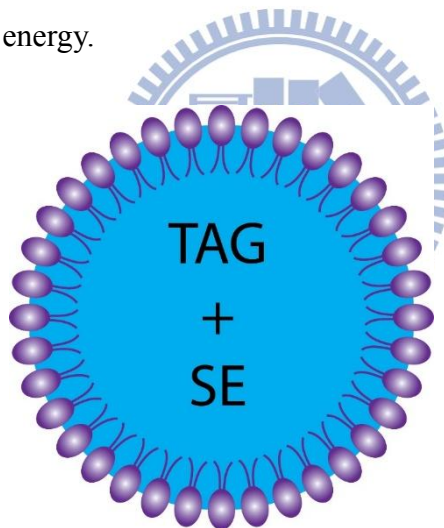


Figure IV-1. Schematic representation of a lipid droplet.

Lipid core (blue) primarily contains TAG and SE which is surrounded by a phospholipid monolayer (purple).

LDs were long considered as a static energy storage units and thus remained the least characterized cytoplasmic organelle. In the past half-decade, however, LDs have come under the spotlight of cell biology. There is now growing evidence that reveals diverse roles and an intrinsically dynamic nature of LDs as a key player in various cellular processes, such as lipid

homeostasis and cell signalling [36]-[41]. It has also been shown that LDs are relevant to many serious health issues, including obesity, type 2 diabetes, and atherosclerosis. Among various functions of LDs, a recently proposed hypothesis that LDs serve to temporarily sequester proteins is thought provoking and might potentially deepen our understanding of LD [42]-[44]. Proteomic studies have detected LD-associated proteins in many cell types [43], [45], which apparently have little to do with lipid metabolism. Those proteins include histones [42], caveolins [46], and perilipin family proteins [47]. Although proteomic analysis is very powerful for identifying and characterizing individual key proteins, biochemical fractionation and purification procedures adopted in LD proteomics are vulnerable to contamination. Moreover, proteomic analysis cannot provide information on spatial localization (distribution) of proteins as well as their temporal evolution. To test whether LDs are both spatiotemporally and functionally associated with proteins (e.g., sequestration), direct evidence needs to be obtained from single living cells using microscopic and imaging techniques.

IV-2. How can Raman microspectroscopy help?

Molecular imaging based on linear/nonlinear Raman spectroscopy has emerged as a promising tool to trace intracellular processes in vivo and at the molecular level. In contrast with commonly employed fluorescence microscopy, Raman-based methods require no exogenous probe to be introduced to cells. Vibrational resonances, which are an inherent property of molecules, give rise to chemical specificity and, hence, enable label-free molecular imaging. Of particular importance is work using coherent anti-Stokes Raman scattering (CARS) microscopy, which has high sensitivity and three-dimensional sectioning capability. The Xie group at Harvard demonstrated video-rate CARS imaging of living cells and tissues [48]. Hellerer et al. [49] also used CARS microscopy to visualize lipid distributions in *Caenorhabditis elegans*. Very recently, Xie and coworkers have further improved image contrast

by using stimulated Raman scattering (SRS) instead of CARS [50], [51]. SRS is, in principle, free from the nonresonant background that always interferes with vibrationally resonant signals in CARS. These nonlinear Raman microscopic studies achieved to date mostly rely on the strong C-H stretch vibrations around 2850 cm^{-1} [48]-[53]. However, C-H stretch images alone do not allow us to directly look into the interplay between LDs and proteins and other organelles. In contrast, Raman microspectroscopy and imaging [28], [54]-[57], although taking longer data acquisition time, provide more extensive and detailed molecular information than CARS microscopy without the need for complicated spectral analysis [58]. Hence we use Raman microspectroscopy and imaging.

IV-3. Stable isotope probing

Since we want to learn spatio-temporal and functional relationships between proteome and lipidome, it is essential to be able to distinguish the biomolecular components that are being actively synthesized from those that already exist. Such a distinction is not possible by ordinary Raman spectroscopy. To achieve this capability, we make use of stable isotopes since isotopic substitution can be of invaluable help in the analysis of vibrational spectra.

Stable-isotope probing (SIP), in which stable isotopes such as ^{13}C and ^{15}N are incorporated in cells as a non-perturbative tracer for RNA [59], DNA [60], and proteins [61], has been widely used for microbial identification. When combined with Raman imaging [8], [62]-[64], the stable-isotope labeling strategy can confer an ability to differentiate between cellular components produced through distinct anabolic pathways and temporal evolutions. This ability arises from the fact that the characteristic frequency (ν) of an oscillator representing a molecular vibration is inversely proportional to the square root of the reduced mass (μ) of the oscillator (**Equation IV-1**).

$$v = \frac{1}{2\pi} \sqrt{\frac{k}{\mu}} \quad \dots \text{Equation IV - 1}$$

In general the force constants (k) are unaltered by isotopic substitution. Hence, the heavier the incorporated isotope, the lower the frequency i.e., redshift in a Raman spectrum (Figure IV-2)[65].

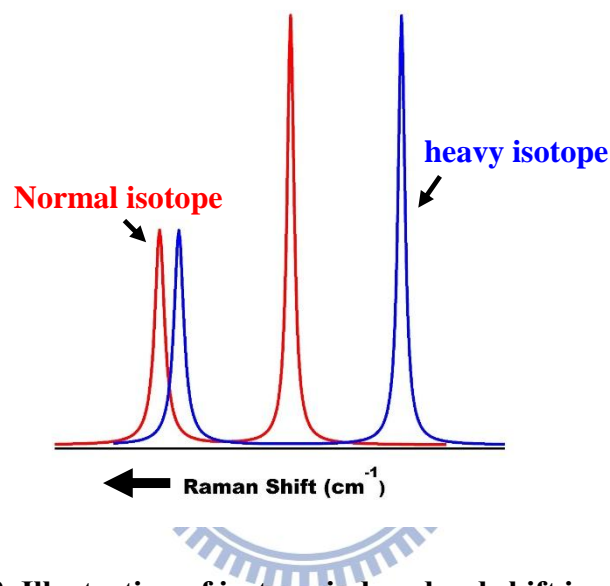


Figure IV-2. Illustration of isotope-induced red shift in a Raman spectrum. The red trace corresponds to a normal isotope and blue to its heavier counterpart.

IV-4. Sample

Raman microspectroscopy is so powerful in that it can be applied to various samples starting from single cells [8], [28], [30], biofilms [3], [27], tissues [48], [66], [67] to small living animals such as mice [68]-[70] and humans [71]. Since our main interest is to study proteome and lipidome together, it is important to study a whole organism. So, in the present study, we chose fission yeast, *Schizosaccharomyces pombe* (*S. pombe*), which is one of the most popular eukaryotic model organisms in molecular and cellular biology, owing to its size. Moreover, LD

biology of yeasts has been extensively studied and a wealth of information is already available.

Main reasons behind choosing fission yeast are summarized as follows:

- a) It is a unicellular rod-shaped eukaryote
- b) Typical size ranges from 3 - 5 μm in diameter and 8 - 15 μm in length
- c) They grow and divide by medial fission forming two equally sized daughter cells which is very suitable for cell cycle research and
- d) Yeasts are shown to form/accumulate lipid droplets at various conditions

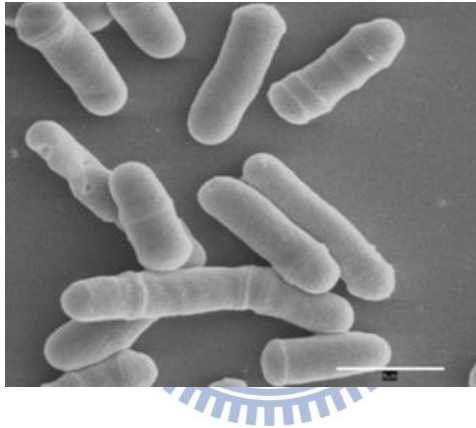


Figure IV-3. Scanning electron micrograph of a fission yeast (*S.pombe*) culture.

Scale bar=10 μm .

Source: The cell cycle. Principles of control. David O Morgan (Jan 1st 2007)

IV-5. Growth of yeast cells in ^{13}C medium

As a first step, to examine whether there are any adverse effects on cell growth caused by heavy carbon isotope (^{13}C), we cultured fission yeast cells in minimal medium with ^{13}C -glucose supplied as a primary carbon source and characterized the growth curve. Briefly, *S. pombe* cells were cultured in both ^{12}C - and ^{13}C -glucose containing Edinburgh Minimal Medium (EMM) broth and the increase of optical densities (OD) with time, taken at 600 nm after 10 times dilution of the culture to avoid saturation at longer time, using a UV-Vis spectrophotometer gives a measure of density of both the cultures. Both cultures showed quite a similar growth characteristics (**Figure IV-4**). The composition of EMM broth is tabulated in **Table IV-1**. Comparison of growth curves in **Figure IV-4** indicates that cells grown in ^{13}C -EMM perform as normal metabolic activities as in ^{12}C -EMM. Thus we can safely say that the use of ^{13}C -glucose instead of ^{12}C -glucose does not affect the growth of yeast cells.

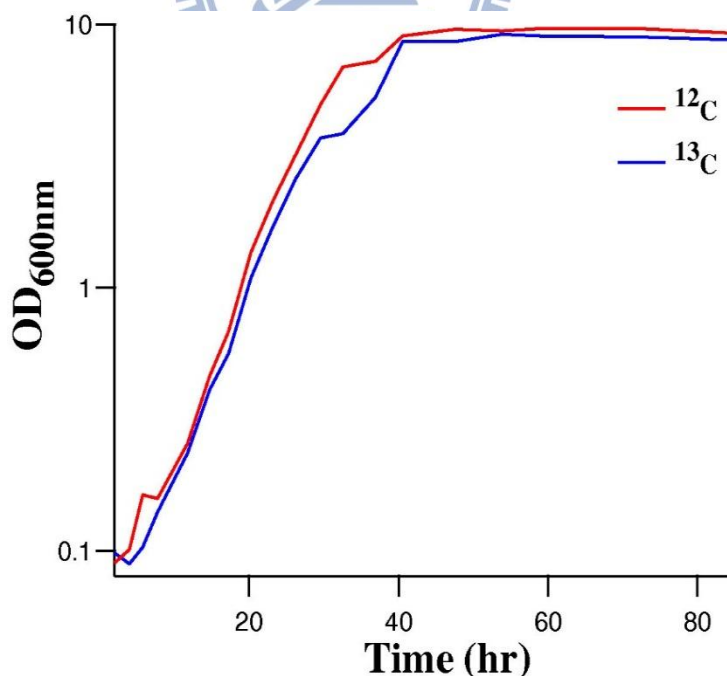


Figure IV-4. Growth curves of fission yeast in ^{12}C - and ^{13}C -glucose containing Edinburgh minimal medium.

Table IV-1. Composition of Edinburgh Minimal Medium.

S. No	Component	Amount (/L)
1	potassium hydrogen phthallate	3 g
2	Na ₂ HPO ₄	2.2 g
3	NH ₄ Cl	5 g
4	glucose	20 g
5	Salts	20 ml
6	Vitamins	1 ml
7	Minerals	0.1ml

IV-6. Stable isotope labeling of fission yeasts

After confirming that ¹³C is harmless, space-resolved Raman spectra from yeast cells grown in ¹²C- and ¹³C-glucose medium were recorded. In ¹²C medium, Raman spectra obtained from cytoplasmic regions are dominated by vibrational bands associated with cellular proteins, [hereafter called protein rich (PR) spectra], which primarily include the backbone amide modes and amino acid side chain modes. From Figure IV-5 (b), it is clear that yeast cells grown in EMM with regular ¹²C-glucose have the amide I mode of proteins at 1654 cm⁻¹, amide III at 1253cm⁻¹, C-H bending modes at 1451 and 1338 cm⁻¹, aromatic ring breathing mode of phenylalanine (Phe) residues at 1003 cm⁻¹ and a tyrosine band at 853 cm⁻¹. Bands between 1040 - 1150 cm⁻¹ and at 916 cm⁻¹ represent the C-C stretching modes. When cells are fed with stable ¹³C isotope containing EMM, several bands show red shift due to heavy isotope effect. Primarily, the amide I and III shift to 1620 and 1237cm⁻¹, respectively. The ring breathing mode of Phe shifts from 1003 to 967 cm⁻¹ and strong tyrosine band appears at 828 cm⁻¹. The C-C stretch modes also show small shifts including the relatively isolated 916 cm⁻¹ band, which shifts to 899 cm⁻¹.

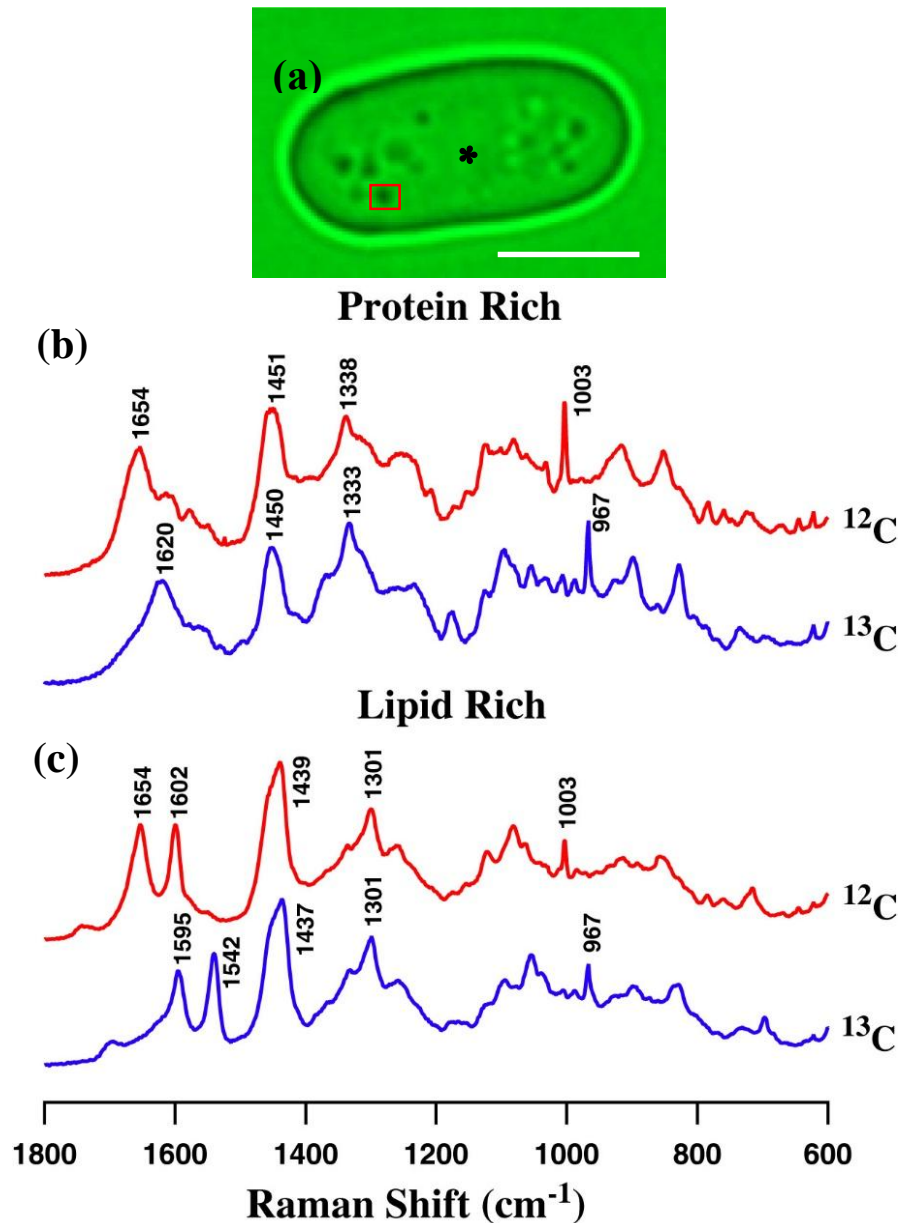


Figure IV-5. (a) Optical image of a typical fission yeast. The transparent region inside the cell indicated by an asterisk is the cytoplasm where protein rich spectra were recorded. The black dot, highlighted by a shown in red square represents LD where lipid rich spectra were measured. Scale bar = $5\mu\text{m}$. (b,c) Space-resolved Raman spectra from yeast grown in ^{12}C and ^{13}C -EMM in protein rich (b) and lipid rich regions (c) to identify vibrational isotope shifts.

Similarly, Raman spectra [called lipid rich (LR) spectra] obtained from LDs are dominated by the C=C stretch of unsaturated lipid chains, C-H bending modes of the hydrocarbon chains, and skeletal C-C stretch modes as shown in **Figure IV-5 (c)**. Obvious red shifts can be observed for the C=C stretch from 1654 to 1595 cm^{-1} and the ergosterol marker band (arising from the C=C diene in-phase stretch of the ring moiety) at 1602 to 1542 cm^{-1} in ^{12}C and ^{13}C media, respectively. The C=O stretch of the ester linkage shifts from 1744 to 1695 cm^{-1} . A band at 716 cm^{-1} ascribed to the phospholipid head group shifts to 697 cm^{-1} . The C-H bending modes, including CH_2 scissors and CH_3 degenerate deformation of the hydrocarbon chains, at 1440/1450 and 1338 cm^{-1} show no appreciable isotope shifts. The in-phase CH_2 twisting mode at 1301 cm^{-1} is observed at the same frequency in both media and is completely insensitive to ^{13}C substitution. All vibrational band shifts observed in the PR and LR spectra are consistent with previous reports [8], [28], [62], [72]. Details of peak position, assignment and ^{13}C isotope effect are tabulated for proteins and lipids in **Table IV-2**.

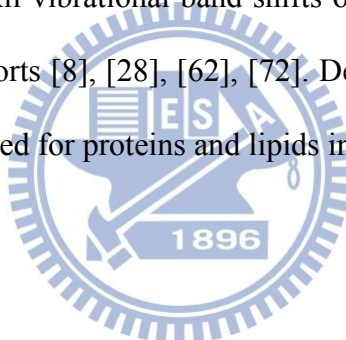


Table IV-2. Peak positions in ^{12}C - and ^{13}C -EMM, molecular component with their tentative assignments

S.No	Peak position in ^{12}C medium (cm^{-1})	Peak position in ^{13}C medium (cm^{-1})	Molecular component	Assignment
1	1654	1620	Protein	Amide I
2	1451	1450	Protein	CH bending
3	1338	1333	Protein	CH_2 deformation
4	1253	1237	Protein	Amide III
5	1003	967	Protein	Phenylalanine
6	853	828	Protein	Tyrosine
7	916	899	Protein	C-C stretch
8	1744	1695	Lipid	C=O str, ester
9	1654	1595	Lipid	C=C stretch
10	1602	1542	Lipid	ergosterol
11	1439	1437	Lipid	CH bending
12	1301	1301	Lipid	In-plane CH_2 twist
13	716	697	Lipid	Phospholipid Head group

IV-7. Selection of marker bands for proteins and lipids

Among all bands in PR spectra, the ^{13}C -shifted Phe bands at 967 cm^{-1} appears in a clean spectral region and represents a strong, distinguishable Raman signal that can be easily detected even in cellular Raman spectra. Thus this band emerges as a potential marker for the ^{13}C incorporation/substitution in newly formed proteins. For similar reasons, the band at 1542 cm^{-1} in LR spectra helps as a marker for the newly synthesized lipids. Additionally, the lipid band at 1301 cm^{-1} , which does not show any shift, can be used as isotope insensitive lipid marker to see total intracellular lipids.

The reason behind not considering C-C stretch modes as a possible marker is due primarily to the fact that these bands are observed in both PR and LR spectra and also because they are present in a highly congested region containing several bands, which makes them complicated for further analysis. Typically, tyrosine residues show a doublet at 853 and 825 cm^{-1} , which arises from the Fermi resonance between the ring breathing vibration and the overtone of an out-of-plane ring-bending vibration. This tyrosine doublet is known to be a strong indicator of the H-bonding strength of the phenolic hydroxyl group [26]. The tyrosine band at 853 cm^{-1} (apparently shifting to 828 cm^{-1} in ^{13}C medium) was not considered as a potential protein marker because it is ambiguous whether the band intensity increase of the 828 cm^{-1} band is really due to ^{13}C isotope substitution or due to change in the H-bonding environment.

IV-8. Bulk experiments

Detailed space- and time-resolved Raman experiments were performed in order to understand the dynamics of ^{13}C incorporation/substitution in lipids and proteins and to observe intermediary spectral features, if any, during the process. Raman spectra characteristic of PR and LR regions that can be free from cell individuality can be best represented by average spectra obtained from measurements on many cells. In light of this, we recorded Raman spectra in both PR and LR regions of 25 randomly picked yeast cells at each time (after washing twice with sterile distilled water) and obtained their averaged spectra as shown in **Figures IV-6 (a)** and **IV-7 (a)**. Pearson correlation coefficients r , calculated using the formula below, for the

$$r = \frac{\sum_{i=1}^n (X_i - \bar{X})(Y_i - \bar{Y})}{\sqrt{\sum_{i=1}^n (X_i - \bar{X})^2} \sqrt{\sum_{i=1}^n (Y_i - \bar{Y})^2}}$$

whole spectrum obtained are very high with

similarity greater than 90% as shown in **Figures IV-6 (b)** and **IV-7 (b)**.

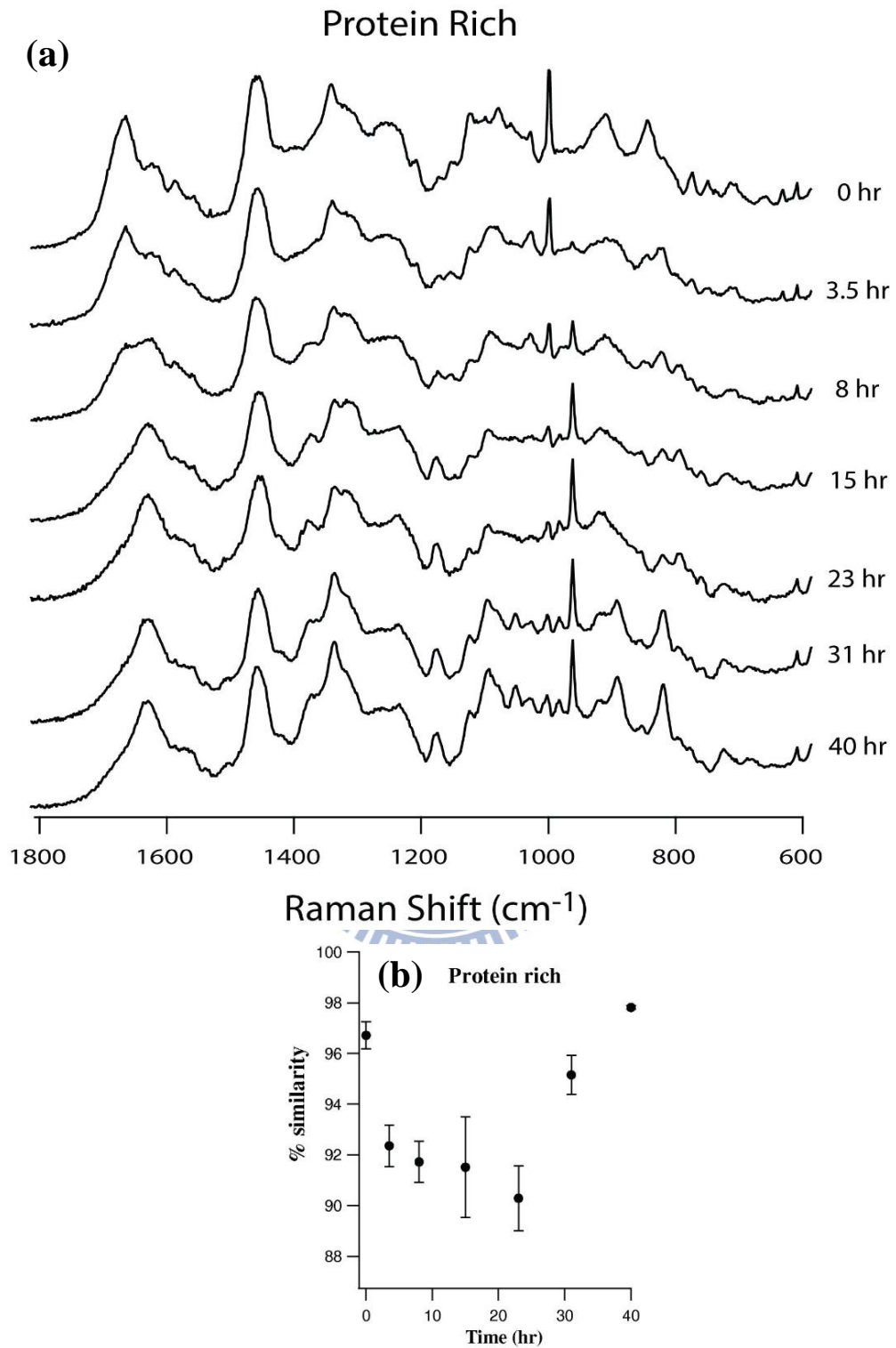


Figure IV-6. (a) Space- and time-resolved Raman spectra showing the evolution of isotope incorporation in PR regions in yeasts, (b) Percentage similarity among PR spectra at each time calculated by Pearson correlation coefficients. Each spectrum is an average of 25 different cells.

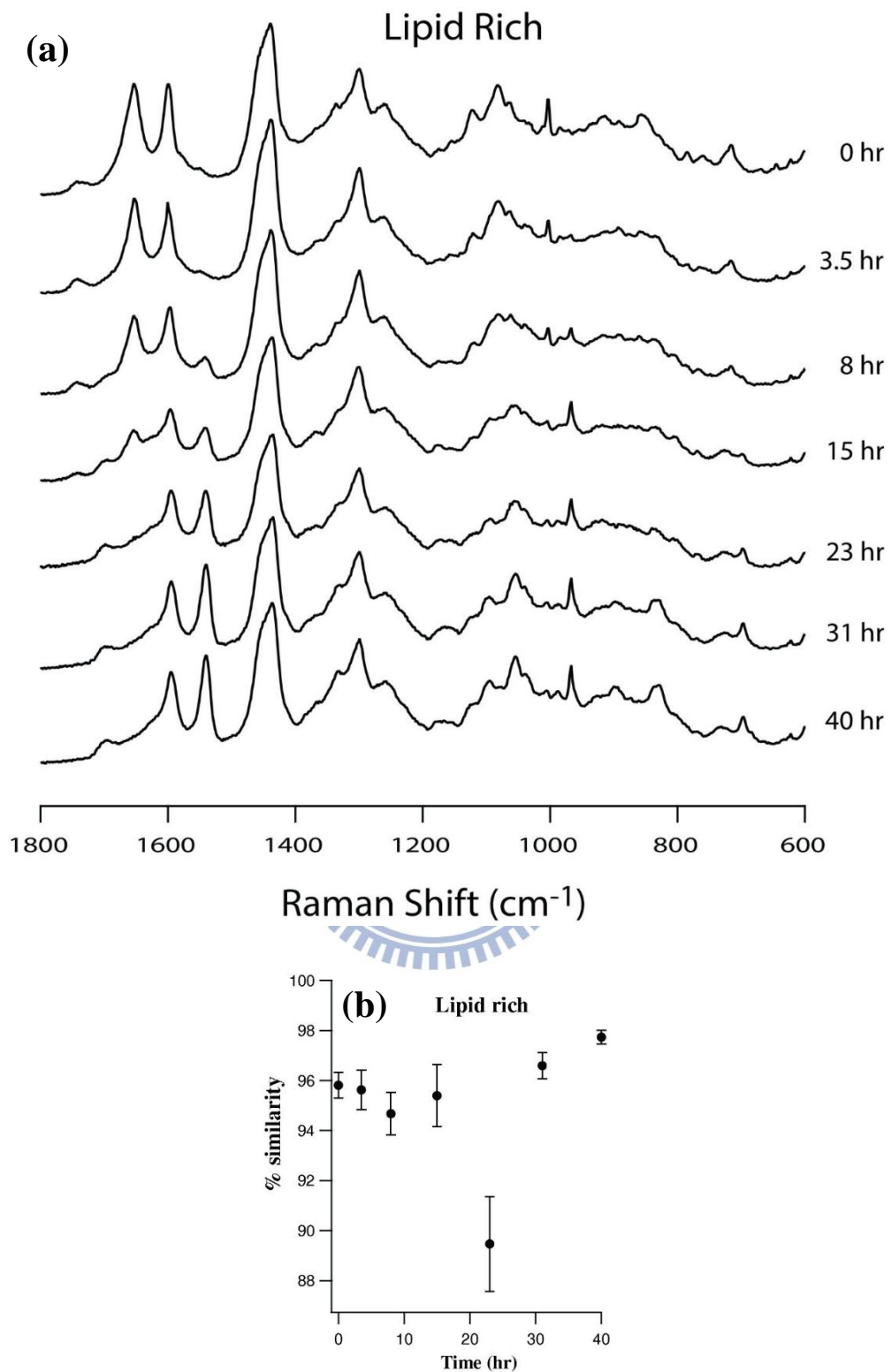


Figure IV-7. (a) Space- and time-resolved Raman spectra showing the evolution of isotope incorporation in LR regions in yeasts, different cells, (b) Percentage similarity among LR spectra at each time calculated by Pearson correlation coefficients.

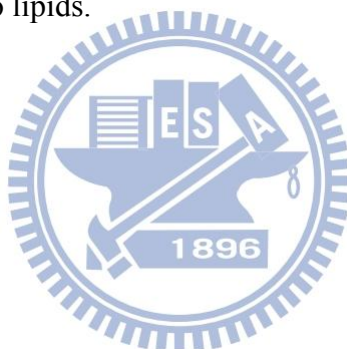
Each spectrum is an average of 25 different cells.

This result shows that the variation between the measurements is small at each time and indeed individual spectra are very close to the averaged one. **Figure IV-8** displays the time evolution of the intensities of several pairs of Raman bands observed in PR and LR spectra. To ascertain the degree of ^{13}C substitution, ring breathing modes of Phe residues (1003 cm^{-1} in ^{12}C & 967 cm^{-1} in ^{13}C) and appearance of 1542 cm^{-1} are used as markers for proteins and lipids, respectively. In general, the doubling time of fission yeasts in EMM broth is somewhere between 2 - 4 hr. Consistent with this time scale, at 3.5 hr, just after 1 generation, the intensities of ^{12}C -amide I band [1654 cm^{-1} , **Figure IV-8 (a)**] and ^{12}C -Phe band [1004 cm^{-1} , **Figure IV-8 (b)**] in PR spectra decrease considerably and at the same time ^{13}C -Phe band at 967 cm^{-1} becomes identifiable, though very weak, indicating active protein synthesis.

Approximately after a couple of generations, (~ 8 hr), appreciable amounts of ^{13}C incorporation can be observed by the presence of equally strong 967 cm^{-1} [see **Figure IV-6 (a)**]. By this time, the proteins in cells are made predominantly from ^{13}C substrates as can be seen from the appearance of the ^{13}C -shifted amide I backbone mode of proteins peaking at 1620 cm^{-1} [**Figure IV-8 (a)**]. ^{12}C content in proteins fades away rapidly with time and eventually becomes negligible in just about 15 hr as indicated by the 1654 cm^{-1} band in **Figure IV-8 (a) & (b)**. Simultaneously, incorporation of ^{13}C in cytoplasmic proteins is $>75\%$ within that period of time and a complete incorporation can be seen within a day.

Similarly, in LR spectra, the ^{13}C marker band at 1542 cm^{-1} (shifting from 1602 cm^{-1}) band becomes identifiable in about 3.5 hr but becomes more obvious only after ~ 8 hr [**Figure IV-8 (c)**]. In order to understand the dynamics of this band, it is also important to know the fate of its complementary band at 1602 cm^{-1} . Interpreting the dynamics of 1602 cm^{-1} band just by looking at the time-resolved spectra is complicated because the C=C stretch band at 1654 cm^{-1} also shifts to 1595 cm^{-1} and interferes with the observation of the 1542 cm^{-1} band. As a result,

the intensity at 1602 cm^{-1} decreases initially, reflecting the actual decrease of the band, but starts increasing from 15 hr because ^{13}C -substituted C=C stretch band comes in [**Figure IV-8 (d)**]. Hence, it is only appropriate to correlate the appearance of the 1542 cm^{-1} band in an indirect manner, with the decay of the 1654 cm^{-1} instead of the 1602 cm^{-1} band. This is why the dynamics of the 1654 and 1542 cm^{-1} bands are coupled together in **Figure IV-8 (c)**. The intensity of the 1542 cm^{-1} band increases with time, whereas that of 1654 cm^{-1} decreases. In lipids, ^{12}C content becomes negligible at 23 hr and incorporation of ^{13}C completes at around 30 hr. By repeating these experiment and looking into the dynamics of the 1654 cm^{-1} band in proteins and lipids, we understand that complete depletion of the ^{12}C -associated bands takes <15 hr for proteins and ~ 24 hr for lipids. In other words, isotope incorporation in proteins occurs at a faster rate when compared to lipids.



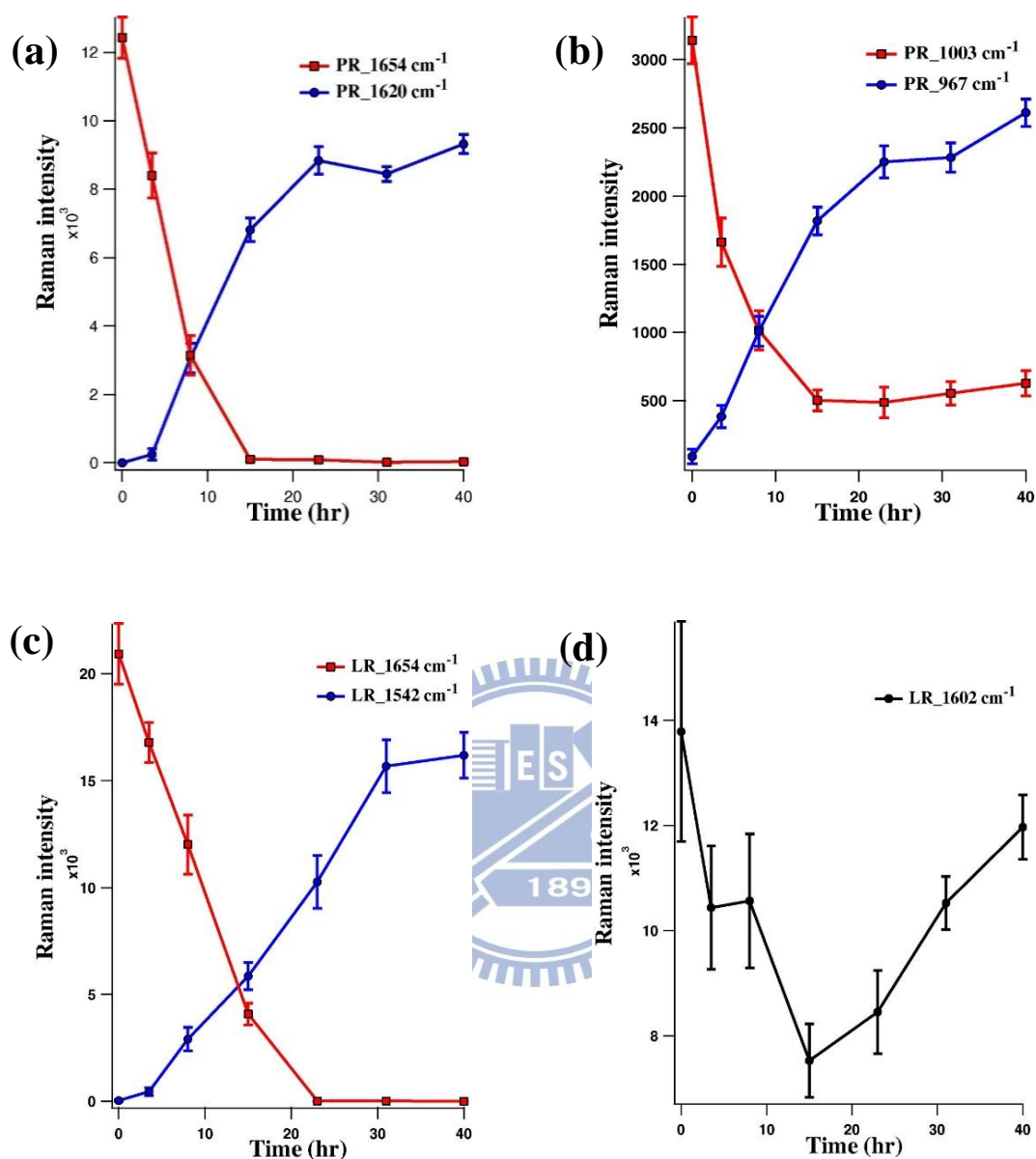


Figure IV-8. ^{13}C incorporation dynamics observed with incubation time in bulk experiments. (a) Amide I bands in PR spectrum at 1654 cm^{-1} (red) and 1620 cm^{-1} (blue) (b) Phenylalanine breathing mode in PR spectrum at 1003 cm^{-1} (red) and 967 cm^{-1} (blue) (c) $^{12}\text{C}=\text{C}$ str at 1654 cm^{-1} (red) and ^{13}C -shifted 1602 at 1542 cm^{-1} (blue) from LR spectrum (d) 1602 cm^{-1} from LR spectrum

IV-9. Single cell Raman imaging

We now have gained a detailed picture of how Raman spectra of the cytoplasm and LD vary as ^{13}C -glucose is assimilated in *S. pombe* cells. However, those data were obtained by averaging behaviours of many different *S. pombe* cells, so they do not provide information on spatial distributions of the cellular components within a single cell and their temporal changes during the course of ^{13}C incorporation. To address these crucial issues, we need to combine the ^{13}C labeling technique with time-lapse Raman imaging on a single *S. pombe* cell.

Here, we use the Phe band to generate protein Raman images since Phe residues are usually abundant in proteins. The Phe band can probe nearly the whole intracellular population of proteins at a given instant. In other words, this Raman band manifests the proteome.

For markers of LDs, we use the bands at 1301 and 1602 cm^{-1} . **Figure IV-9** shows time-lapse Raman images over 37 hr, constructed at 1003, 967, 1301, and 1602 cm^{-1} , of a single stationary-phase *S. pombe* cell with green fluorescence protein (GFP)-labeled mitochondria fed with ^{13}C -glucose. All the four Raman images at a given measurement time were obtained simultaneously from one two-dimensional scan of the cell. Each Raman image is represented in a pseudocolor scale (red, magenta, cyan, yellow, or rainbow). For example, a red pseudocolor scale in which the highest intensities appear white, the moderate appear red, and the lowest appear black is used for the Raman images at 1003 cm^{-1} [**Figure IV-9 (c)**].

Also shown are bright-field optical micrographs [**Figure IV-9 (a)**] and GFP fluorescence images [**Figure IV-9 (b)**] of the *S. pombe* cell. The optical micrographs are silent about molecular distribution, although LDs of ~ 0.1 μm size can be seen as black dots (as indicated by arrows at 31 hr). The GFP image clearly visualizes mitochondrial distribution at each time.

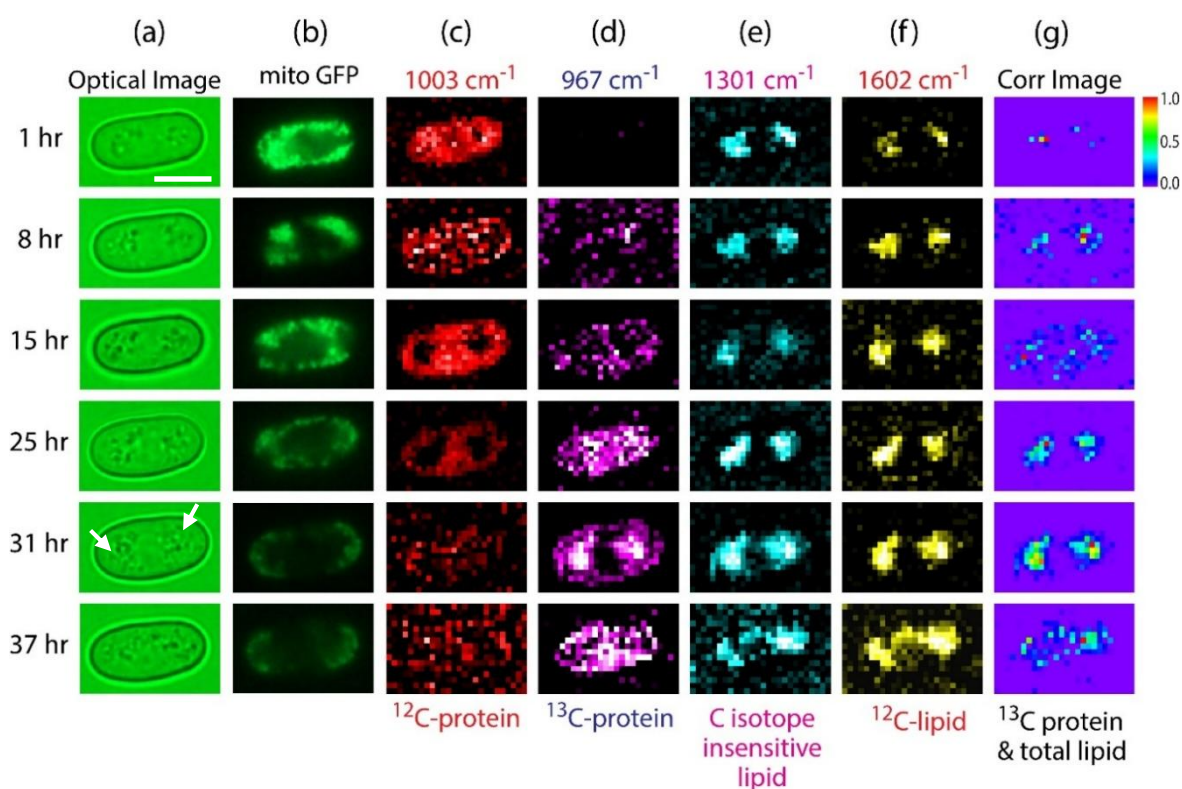


Figure IV-9. Time-lapse multimode Raman imaging of a single living *S.pombe* cell grown ^{13}C -glucose containing medium.

(a) Bright-field optical images of the target cell. Arrows at 31 hr indicate the regions where there are many lipid droplets. LDs are identified as black dots. (b) GFP fluorescence images of mitochondria of the cell. (c–f) Raman images constructed at 1003 (Phe breathing mode of ^{12}C -proteins), 967 (Phe breathing mode of ^{13}C -substituted proteins), 1301 (in-plane CH_2 twist of lipids), and 1602 cm^{-1} . The scale bar in (a) measures 5 μm and also applies to the other images. (g) Correlation images between (d) and (e). The correlation coefficient at each pixel was computed using the equation given in the text

Let us examine first a pair of the time-lapse Raman images of the Phe band for proteins. The Raman images at 1003 cm^{-1} [Figure IV-9 (c)] represent the distribution of Phe-containing proteins that are originally present within the *S. pombe* cell when we started the imaging experiment, whereas those at 967 cm^{-1} [Figure IV-9 (d)] map the distribution of newly formed proteins using exogenous ^{13}C substrate. One hour after inoculation in ^{13}C -EMM, proteins are

distributed homogeneously across the cell and ^{13}C is not yet incorporated into proteins. As time progresses, the ^{12}C content in proteins is depleted particularly in two regions where many LDs are seen. After 31 hr, the intensity of the 1003 cm^{-1} band decreases to a noise level. Protein synthesis machinery, which is known to be continuously operating, utilizes ^{13}C substrate taken up in the cell to fulfill its mission. As a result, the concentration of ^{13}C -labeled proteins probed at 967 cm^{-1} gradually increases [Figure IV-9 (d)], which is consistent with the results of the bulk experiments. In sharp contrast with the existing ^{12}C proteins, newly formed ^{13}C -labeled proteins show a heterogeneous distribution pattern with time (at 25 and 31 hr), and more importantly, are localized to the region where lipids are highly concentrated, i.e., LDs. At 37 hr, the distribution of ^{13}C -labeled proteins becomes homogeneous again.

Next we look into the Raman images of lipids at 1301 cm^{-1} [Figure IV-9 (e)]. Lipids are localized near two ends of the cell [54] at all measurement times except for 37 hr, at which the distribution appears to be more uniform. In addition, the total concentration of lipids increases after 15 hr. The Raman images at 1602 cm^{-1} [Figure IV-9 (f)] markedly resemble those at 1301 cm^{-1} . This resemblance is not surprising because the 1602 cm^{-1} band is associated with ergosterol [73], which is a fragment of sterol esters, a major constituent of the LD core. According to our bulk experiments, the 1301 cm^{-1} band shows no ^{13}C shift, whereas the 1602 cm^{-1} band shows a 60 cm^{-1} shift. In the imaging experiment, however, the total intensity of the 1602 cm^{-1} band within the *S. pombe* cell does not decrease at all with time. This result suggests that a majority of lipids are synthesized by consuming ^{12}C substrate available within the cell.

We have assigned above the LR regions in the cell predominantly to LDs. This assignment is supported by the following pieces of evidence. First, in yeast, mitochondria along with LDs, are known to be the major organelle where lipids are abundant, so the Raman images shown in Figure IV-9 (e) could be associated with mitochondria rather than with LDs.

However, the GFP-labeled mitochondrial images [**Figure IV-9 (b)**] do not accord with the lipid images [**Figure IV-9 (e)**]. Because the GFP images were acquired just before the Raman measurement, it is unlikely that considerable intracellular reorganization of mitochondria occurred between the two measurements. Therefore, we confirm that mitochondria cannot account for the distribution pattern of lipids shown in **Figure IV-9 (e)**. Second, LDs provide a unique environment suitable for the storage of hydrophobic sterol esters, which are neither soluble in the aqueous cytosol nor present as typical lipid bilayer membranes [74]. The steroid part of the major class of sterol esters in yeast is ergosterol. As mentioned above, a recent Raman spectroscopic study on LD fractions isolated from the tetraploid W4 strain of yeast suggests that ergosterol is the prominent contributor to the 1602 cm⁻¹ band [73].

Because the lipid band at 1301 cm⁻¹ and the 1602 cm⁻¹ band exhibit a virtually identical distribution at any measurement time, it is reasonable to link them to the same organelle, most likely LDs. At 25 and 31 hr, the distribution patterns of the Raman images associated with LDs [**Figures IV-9 (e), (f)**] correlate very well with that of the protein image at 967 cm⁻¹ [**Figure IV-9 (d)**], both showing high intensities near the two ends of the cell. To examine this colocalization phenomenon quantitatively, we performed structural cross-correlation image analysis for the Raman images of ¹³C-labeled proteins [**Figure IV-9 (d)**] and lipids [**Figure IV-9 (e)**]. The correlation image analysis compares signal intensities of two images on a pixel-by-pixel basis, yielding the correlation coefficient C_{ij} at each pixel which can be calculated as is shown in the equation below [75], [76].

$$C_{ij} = \frac{(a_{ij}/a_{max})(b_{ij}/b_{max})}{[(a_{ij}/a_{max})(b_{ij}/b_{max})]_{max}}$$

Here, a_{ij} and b_{ij} represent intensities at the (i,j) th pixel of the two images a and b. The correlation images so obtained show remarkably high correlation in the LR region only at 25

and 31 hr [**Figure IV-9 (g)**]. The correlation image at 37 hr reveals a less pronounced correlation between the 967 and 1301 cm^{-1} Raman images, with a more diffuse pattern compared with those at 25 and 31 hr. Another important point to note is that the colocalization phenomenon seems to be synchronized with the increase of lipid concentration [**Figure IV-9 (e), (g)**]. In fact, the time when the correlation becomes evident coincides with the onset of the lipid increase. This finding provides a clue to interpret the colocalization behavior from a physiological viewpoint of the *S. pombe* cell.

Then, we asked whether the colocalization phenomenon is accidental or specific to the *S. pombe* cell we chose. To address this question, we performed time-lapse Raman imaging on another three *S. pombe* cells. Raman images of the protein and lipid marker bands (967 and 1301 cm^{-1} respectively) for the three cells at later stages after inoculation into ^{13}C -EMM are shown in **Figure IV-10**, together with their optical images, GFP images, and correlation images. The three cells differ in strain and/or growth phase from which the cell was chosen: namely, the same strain with GFP-labeled mitochondria as in **Figure IV-9** [**Figure IV-10 (a)**], a different wild-type strain (PR110) at early-log phase [**Figure IV-10 (b)**], and yet another wild-type strain (BCRC21605) at mid-log phase [**Figure IV-10 (c)**]. Although we were unable to acquire a statistically significant number of single-cell data (say $n=50$), all the cells studied ($n = 4$) showed, to a greater or lesser extent, a similar tendency of colocalization of newly formed proteins and LDs at similar time scales, irrespective of strain and growth phase.

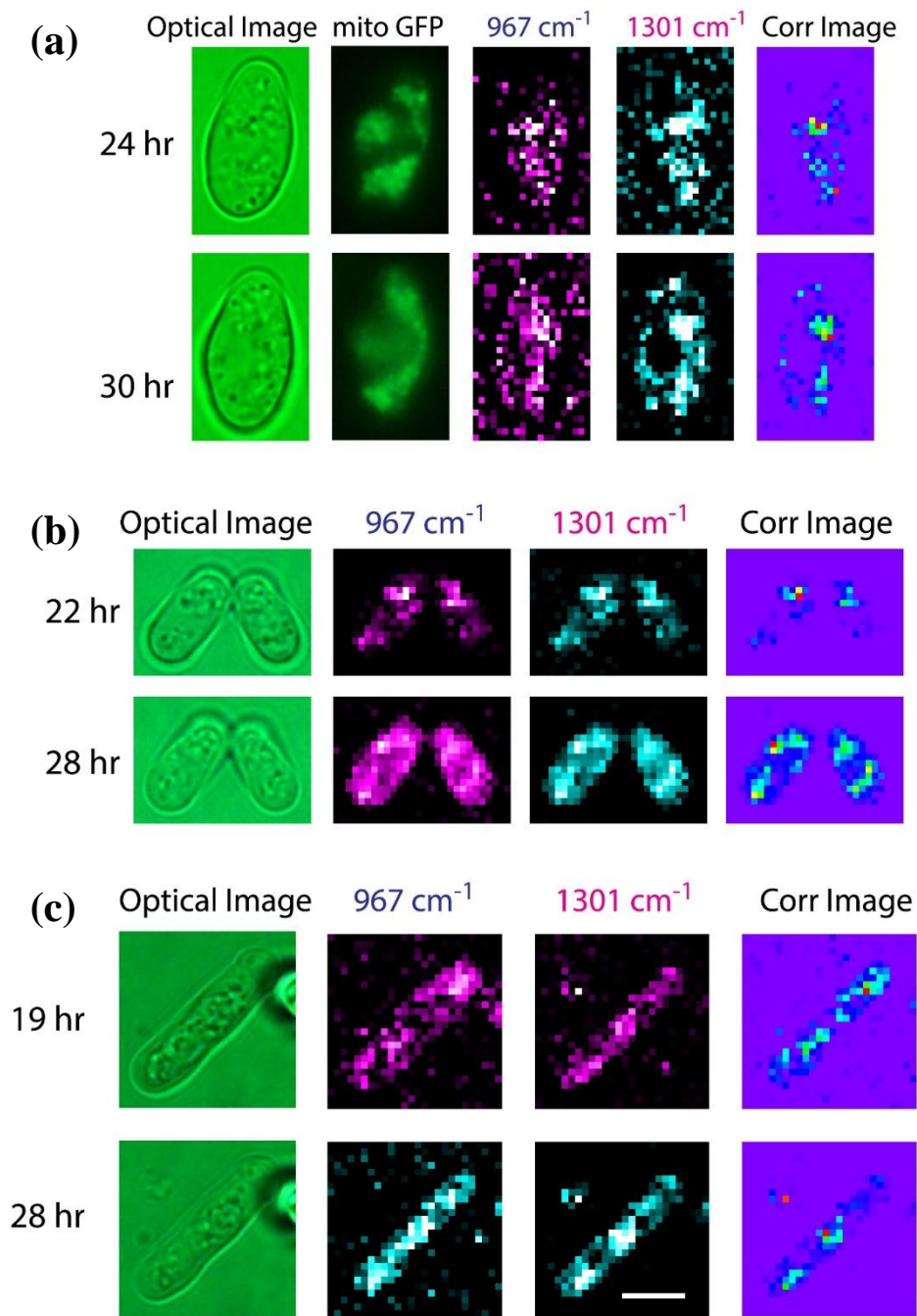


Figure IV-10. Time-lapse Raman imaging of other single living *S. pombe* cells grown in ^{13}C -glucose containing medium.

(a) The same GFP-labeled strain as in Figure IV-9. From left to right, the optical image, GFP image, Raman images at 967 and 1301 cm^{-1} , and their correlation images are shown. (b) A different wild-type strain (PR110) taken from early-log phase. (c) Yet another wild-type strain (BCRC21605) taken from mid-log phase. The scale bar measures 5 μm and also applies to the other images.

IV-10. Biological implications of this colocalization phenomenon

As indicated by the Raman images of the 967 cm^{-1} band in **Figures IV-9 (d) and IV-10**, the sole carbon source in the medium (^{13}C glucose) is almost exhausted by ~ 20 hr because of its incorporation in the cell, putting the yeast cell in starvation. It has been shown that, under conditions of nutrition deprivation, LDs increase in the cell to store more TAG for energy [77]. As a consequence, when the cell starts to starve, proteins involved in lipid formation might be urgently synthesized from the remaining ^{13}C -substrate inside the cell and recruited to the site of action (i.e., LDs). This recruitment results in the localization of ^{13}C -substituted proteins to LDs in the time frame of 20–30 hr. In a generally accepted view, LD-associated proteins reside not in the core composed of neutral lipids but on the surface composed of phospholipid monolayer or in the close vicinity of LDs. We presume that this is also the case with the localized proteins that we observed, but our spatial resolution of ~ 500 nm is not high enough to experimentally determine their more precise locations. Recent studies suggest that LDs might also sequester some denatured proteins until they are handed over to the cellular degradation machinery or temporarily store proteins for later use [42]-[44]. Apparently, our findings do not favour this mechanism, illustrating that LDs are indeed involved in a variety of dynamic intracellular processes. Although more comprehensive studies are needed, the present study has shed an experimental light on such multifaceted and perhaps interrelated roles of LDs in relation to intracellular proteins.

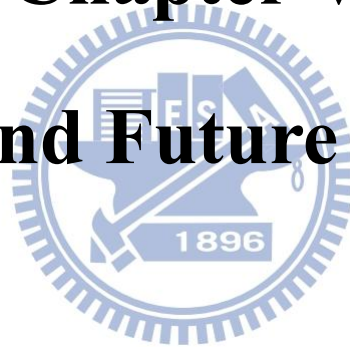
IV-11. Conclusion

In summary, we have shown, by using *in vivo* time-lapse Raman imaging coupled with stable-isotope (^{13}C) labeling, that proteins synthesized via anabolic incorporation of ^{13}C -glucose into a single *S. pombe* cell are localized to LDs. Although protein localization to other organelles, such as the nucleus, mitochondria, and the endoplasmic reticulum, in the fission yeast *S. pombe* was previously revealed by using a combination of cloning and fluorescence microscopy [78], the localization to LDs so far has not been observed by any other experimental methods. Because the fission yeast is the fundamentally most important model organism, our results not only provide direct evidence for the colocalization phenomenon along with the previous work on *Drosophila* embryos [42], but also suggest that it might be conserved in many organisms. The colocalization phenomenon we observed seems to occur when the intracellular concentration of lipids in the form of droplets is increased (e.g., by starvation).

The conventional biological approach excels in revealing the identity and characteristic function of individual proteins associated with LDs, but it still remains challenging to study the proteome and other intracellular components at the same time. Such studies would require many different probes to be introduced to the target cell, very likely resulting in considerable perturbation of cell physiology. In contrast, at the cost of the specificity to individual proteins, Raman spectroscopy can look at the proteome simultaneously (all protein molecules containing Phe residues in the present case) without the need for tagging them with dye molecules. Moreover, it offers both space and time specificity, which cannot be achieved by imaging mass spectrometry [79], another promising tool for bioimaging. Together, stable isotope-labeled Raman imaging should be a powerful, complementary addition to the arsenal of lipid droplet biology.

Chapter V

Summary and Future Perspectives



We have successfully demonstrated the usefulness of Raman micro-spectroscopy in advancing our knowledge pertaining to complex biological phenomena. We first did exploratory studies of bacterial biofilms.

In structured communities of bacteria known as biofilms, a variety of biomolecules have been shown to play a unique role as signals and/or regulators in biofilm formation. In this study, we detected high levels of the amino acid leucine (leucine pool), for the first time, within microcolonies in a 30-h-old *Escherichia coli* biofilm by Raman imaging. Localization of leucine revealed by multifrequency Raman images indicates leucine accumulation during the early stage of the *E. coli* biofilm formation, which may have resulted from physiological environment-specific metabolic adaptation. With our results, we clearly demonstrate that our label-free Raman imaging method provides a useful platform for directly identifying still unknown natural products produced in biofilms as well as for visualizing heterogeneous distributions of biofilm constituents *in situ*.

Then we attempted to test a much debated hypothesis that lipid droplets are intimately associated with intracellular proteins since there is little direct evidence by molecular level studies in living cells. To put an end to this debate, we strategically combined *in vivo* time-lapse Raman imaging with stable isotope labeling to study spatiotemporal relations between lipids and proteins in single fission yeasts. Our results show that the proteins newly synthesized from incorporated ^{13}C -substrate are localized specifically to lipid droplets as the lipid concentration within the cell increases. We demonstrate that the present method offers a unique platform for proteome visualization without the need for tagging individual proteins with fluorescent probes.

Stable isotope labelling coupled with Raman spectroscopy is so powerful in that, it is now possible to address some very fundamental questions as to whether metabolic pathways are affected by isotopes. We are now attempting to elucidate any preferential use of a particular isotope in yeast metabolic pathways.

References

- [1]J. Watson and F. Crick, “Molecular structure of nucleic acids,” *Nature*, vol. 171, no. 4356, pp. 737-738, Apr. 1953.
- [2]H. Liu, M. Jan, C. Chou, P. Chen, and N. Ke, “Is Green Fluorescent Protein Toxic to the Living Cells?,” *Biochemical and Biophysical Research Communications*, vol. 260, no. 3, pp. 712-717, Jul. 1999.
- [3]H. N. Noothalapati Venkata, N. Nomura, and S. Shigeto, “Leucine pools in Escherichia coli biofilm discovered by Raman imaging,” *Journal of Raman Spectroscopy*, vol. 42, no. 11, pp. 1913-1915, Nov. 2011.
- [4]H. N. Noothalapati Venkata and S. Shigeto, “Stable Isotope-Labeled Raman Imaging Reveals Dynamic Proteome Localization to Lipid Droplets in Single Fission Yeast Cells,” *Chemistry & Biology*, vol. 19, no. 11, pp. 1373-1380, Nov. 2012.
- [5]S. Ask, P. Barrillon, A. Braem, C. Cheiklali, I. Efthymiopoulos, D. Fournier, C. Taille, B. Girolamo, P. Grafstrom, C. Joram, M. Haguener, V. Hedberg, B. Lavigne, A. Maio, A. Mapelli, U. Mjörnmark, P. Puzo, M. Rijssenbeek, J. Santos, J. Saraiva, H. Stenzel, M. Thioye, E. Valladolid, and V. Vorobel, “Luminosity measurement at ATLAS—Development, construction and test of scintillating fibre prototype detectors”, *Nuclear Instruments and Methods in Physics Research Section A: Accelerators, Spectrometers, Detectors and Associated Equipment*, vol. 568, no. 2, pp. 588-600, Dec. 2006.
- [6]Y. Lin, Y. Huang, G. Wang, T. J. Tzeng, and D. B. Chrisey, “Effect of laser fluence on yeast cell viability in laser-assisted cell transfer”, *Journal of Applied Physics*, vol. 106, no. 4, p. 043106, Jan. 2009.
- [7]C. Huang, M. Ando, H. Hamaguchi, and S. Shigeto, “Disentangling dynamic changes of multiple cellular components during the yeast cell cycle by in vivo multivariate Raman imaging.”, *Analytical Chemistry*, vol. 84, no. 13, pp. 5661-8, Jul. 2012.

- [8]H. van Manen, A. Lenferink, and C. Otto, “Noninvasive Imaging of Protein Metabolic Labeling in Single Human Cells Using Stable Isotopes and Raman Microscopy”, *Analytical Chemistry*, vol. 80, no. 24, pp. 9576-9582, Dec. 2008.
- [9]M. Okuno, H. Kano, P. Leproux, V. Couderc, J. R. Day, M. Bonn, and H. Hamaguchi, “Quantitative CARS Molecular Fingerprinting of Single Living Cells with the Use of the Maximum Entropy Method”, *Angewandte Chemie International Edition*, vol. 49, no. 38, pp. 6773-6777, Sep. 2010.
- [10]M. Ando, M. Sugiura, H. Hayashi and H. Hamaguchi, “1064 nm Deep Near-Infrared (NIR) Excited Raman Microspectroscopy for Studying Photolabile Organisms”, *Applied spectroscopy*, vol.65, no. 5, pp. 488-492, Nov. 2011.
- [11]H. Jones, Roth, and W. Sanders, “Electron microscopic study of a slime layer”, *Journal of Bacteriology*, vol. 99, no. 1, pp316-325, Jan. 1969.
- [12]WG. Characklis, “Attached microbial growths-II. Frictional resistance due to microbial slimes”, *Water Research*, vol. 7, no. 9, p. 1249, Jan. 1973.
- [13]JW. Costerton, GG. Geesy and KJ. Cheng, “How bacteria stick”, *Scientific American*, vol. 238, no. 1, p. 86, Jan. 1978.
- [14]J. Costerton, P. Stewart, and E. Greenberg, “Bacterial biofilms: a common cause of persistent infections”, *Science*, vol. 284, pp. 1318-1322, May. 1999.
- [15]D. Davies, “Understanding biofilm resistance to antibacterial agents”, *Nature Reviews Drug Discovery*, vol. 2, no. 2, pp. 114-122, Jan. 2003.
- [16]V. Lazarova and J. Manem, “Biofilm characterization and activity analysis in water and wastewater treatment”, *Water Research*, vol. 29, no. 10, pp. 2227-2245, Feb. 1995.
- [17]R. Singh, D. Paul, and R. K. Jain, “Biofilms: implications in bioremediation”, *Trends in Microbiology*, vol. 14, no. 9, pp. 389-397, Sep. 2006.
- [18]E. Karatan and P. Watnick, “Signals, Regulatory Networks, and Materials That Build and Break Bacterial Biofilms”, *Microbiology and Molecular Biology Reviews*, vol. 73, no. 2, pp. 310-347, Jun. 2009.

- [19]C. Whitchurch, T. Tolker-Nielsen, P. Ragas, and J. Mattick, “Extracellular DNA required for bacterial biofilm formation”, *Science*, vol. 295, pp. 1487, Feb. 2002.
- [20]Yormiar, M. Allesen-Holm, K. B. Barken, L. Yang, M. Klausen, J. S. Webb, S. Kjelleberg, S. Molin, M. Givskov, and T. Tolker-Nielsen, “A characterization of DNA release in *Pseudomonas aeruginosa* cultures and biofilms”, *Molecular Microbiology*, vol. 59, no. 4, pp. 1114-1128, Feb. 2006.
- [21]K. C. Rice, E. E. Mann, J. L. Endres, E. C. Weiss, J. E. Cassat, M. S. Smeltzer, and K. W. Bayles, “The *cidA* murein hydrolase regulator contributes to DNA release and biofilm development in *Staphylococcus aureus*”, *Proceedings of the National Academy of Sciences*, vol. 104, no. 19, pp. 8113-8118, May 2007.
- [22]I. Kolodkin-Gal, D. Romero, S. Cao, J. Clardy, R. Kolter, and R. Losick, “D-Amino Acids Trigger Biofilm Disassembly”, *Science*, vol. 328, no. 5978, pp. 627-629, Apr. 2010.
- [23]P. Stoodley, K. Sauer, and D. Davies, “Biofilms as complex differentiated communities”, *Annual Reviews in Microbiology*, vol. 56, pp. 187-209, Apr. 2002.
- [24]K. Sauer, A. K. Camper, G. D. Ehrlich, J. W. Costerton, and D. G. Davies, “*Pseudomonas aeruginosa* Displays Multiple Phenotypes during Development as a Biofilm”, *Journal of Bacteriology*, vol. 184, no. 4, pp. 1140-1154, Feb. 2002.
- [25]M. Wagner, N. P. Ivleva, C. Haisch, R. Niessner, and H. Horn, “Combined use of confocal laser scanning microscopy (CLSM) and Raman microscopy (RM): Investigations on EPS – Matrix”, *Water Research*, vol. 43, no. 1, pp. 63-76, Jan. 2009.
- [26]M. N. Siamwiza, R. C. Lord, M. C. Chen, T. Takamatsu, I. Harada, H. Matsuura, and T. Shimanouchi, “Interpretation of the doublet at 850 and 830 cm^{-1} in the Raman spectra of tyrosyl residues in proteins and certain model compounds.”, *Biochemistry*, vol. 14, no. 22, pp. 4870-6, Nov. 1975.
- [27]N. P. Ivleva, M. Wagner, H. Horn, R. Niessner, and C. Haisch, “Towards a nondestructive chemical characterization of biofilm matrix by Raman microscopy”, *Analytical and Bioanalytical Chemistry*, vol. 393, no. 1, pp. 197-206, Jan. 2009.
- [28]Y. Huang, T. Karashima, M. Yamamoto, and H. Hamaguchi, “Molecular-level investigation

of the structure, transformation, and bioactivity of single living fission yeast cells by time- and space-resolved Raman spectroscopy.”, *Biochemistry*, vol. 44, no. 30, pp. 10009-19, Aug. 2005.

[29]J. W. Chan, L. C. Laboratory, S. C. Davis, L. L. Laboratory, H. Winhold, M. H. Corzett, Materials, J. M. Ulloa, M. Cosman, R. Balhorn, T. Huser, and D. D. California, “Monitoring dynamic protein expression in living E. coli. Bacterial cells by laser tweezers Raman spectroscopy”, *Cytometry Part A*, vol. 71, no. 7, pp. 468-474, Jul. 2007.

[30]C. Xie and Y. Li, “Confocal micro-Raman spectroscopy of single biological cells using optical trapping and shifted excitation difference techniques”, *Journal of Applied Physics*, vol. 93, no. 5, p. 2982, Jan. 2003.

[31]N. P. Ivleva, M. Wagner, H. Horn, R. Niessner, and C. Haisch, “In Situ Surface-Enhanced Raman Scattering Analysis of Biofilm”, *Analytical Chemistry*, vol. 80, no. 22, pp. 8538-8544, Nov. 2008.

[32]N. P. Ivleva, M. Wagner, A. Szkola, H. Horn, R. Niessner, and C. Haisch, “Label-Free in Situ SERS Imaging of Biofilms”, *The Journal of Physical Chemistry B*, vol. 114, no. 31, pp. 10184-10194, Aug. 2010.

[33]J. Valle, S. Da Re, S. Schmid, D. Skurnik, R. D'Ari, and J. -. Ghigo, “The Amino Acid Valine Is Secreted in Continuous-Flow Bacterial Biofilms”, *Journal of Bacteriology*, vol. 190, no. 1, pp. 264-274, Dec. 2007.

[34]D. Rowley, “Inhibition of E. coli Strains by Amino-Acids”, *Nature*, vol. 171, no. 4341, pp. 80-81, Jan. 1953.

[35]M. Felice, M. Levinthal, and M. Iaccarino, “Growth inhibition as a consequence of antagonism between related amino acids: effect of valine in Escherichia coli K-12.”, *Microbiological Reviews*, vol. 43, no. 1, pp. 42-58, Mar. 1979.

[36]M. Digel, R. Ehehalt, and J. Füllekrug, “Lipid droplets lighting up: Insights from live microscopy”, *FEBS letters*, vol. 584, no. 11, pp. 2168-2175, Jun. 2010.

[37]T. Fujimoto and Y. Ohsaki, “Cytoplasmic Lipid Droplets”, *Annals of the New York Academy of Science*, vol. 1086, pp. 104-115, Jan. 2006.

[38]S. Martin, R. G. Parton, and R. G. Martin, “Lipid droplets: a unified view of a dynamic

organelle”, *Nature Reviews Molecular Cell Biology*, vol. 7, no. 5, pp. 373-378, Mar. 2006.

[39]S. Murphy, S. Martin, and R. G. Parton, “Lipid droplet-organelle interactions; sharing the fats”, *Biochimica et Biophysica Acta (BBA) - Molecular and Cell Biology of Lipids*, vol. 1791, no. 6, pp. 441-447, Jun. 2009.

[40]C. Thiele and J. Spandl, “Cell biology of lipid droplets”, *Current opinion in cell biology*, vol. 20, no. 4, pp. 378-385, Aug. 2008.

[41]T. C. Walther and R. V. Farese, “The life of lipid droplets”, *Biochimica et Biophysica Acta (BBA) - Molecular and Cell Biology of Lipids*, vol. 1791, no. 6, pp. 459-466, Jun. 2009.

[42]S. Cermelli, Y. Guo, S. P. Gross, and M. A. Welte, “The Lipid-Droplet Proteome Reveals that Droplets Are a Protein-Storage Depot”, *Current Biology*, vol. 16, no. 18, pp. 1783-1795, Sep. 2006.

[43]B. D. Hodges and C. C. Wu, “Proteomic insights into an expanded cellular role for cytoplasmic lipid droplets”, *The Journal of Lipid Research*, vol. 51, no. 2, pp. 262-273, Jan. 2010.

[44]M. A. Welte, “Proteins under new management: lipid droplets deliver”, *Trends in cell biology*, vol. 17, no. 8, pp. 363-369, Aug. 2007.

[45]K. Grillitsch, M. Connerth, H. Köfeler, T. N. Arrey, B. Rietschel, B. Wagner, M. Karas, and G. Daum, “Lipid particles/droplets of the yeast *Saccharomyces cerevisiae* revisited: Lipidome meets Proteome”, *Biochimica et Biophysica Acta (BBA) - Molecular and Cell Biology of Lipids*, vol. 1811, no. 12, pp. 1165-1176, Dec. 2011.

[46]A. Pol, S. Martin, M. A. Fernandez, C. Ferguson, A. Carozzi, R. Luetterforst, C. Enrich, R. G. Parton, and A. Pol, “Dynamic and Regulated Association of Caveolin with Lipid Bodies: Modulation of Lipid Body Motility and Function by a Dominant Negative Mutant”, *Molecular Biology of the Cell*, vol. 15, no. 1, pp. 99-110, Nov. 2003.

[47]D. Brasaemle, “Thematic review series: adipocyte biology. The perilipin family of structural lipid droplet proteins: stabilization of lipid droplets and control of lipolysis”, *Journal of lipid research*, vol. 48, pp. 2547-2559, Jan. 2007.

[48]C. L. Evans, E. O. Potma, M. Puorishaag, D. Cote, C.P. Lin and X. S. Xie, “Chemical

imaging of tissue in vivo with video-rate coherent anti-Stokes Raman scattering microscopy”, *Proceedings of the National Academy of Sciences*, vol. 102, no. 46, pp. 16807-16812, Nov. 2005.

[49]T. Hellerer, C. Axang, C. Brackmann, P. Hillertz, M. Pilon, and A. Enejder, “Monitoring of lipid storage in *Caenorhabditis elegans* using coherent anti-Stokes Raman scattering (CARS) microscopy”, *Proceedings of the National Academy of Sciences*, vol. 104, no. 37, pp. 14658-14663, Sep. 2007.

[50]C. W. Freudiger, W. Min, G. R. Holtom, B. Xu, M. Dantus, and X. S. Xie, “Highly specific label-free molecular imaging with spectrally tailored excitation-stimulated Raman scattering (STE-SRS) microscopy”, *Nature Photonics*, vol. 5, no. 2, pp. 103-109, Jan. 2011.

[51]B. G. Saar, C. W. Freudiger, J. Reichman, C. M. Stanley, G. R. Holtom, and X. S. Xie, “Video-Rate Molecular Imaging in Vivo with Stimulated Raman Scattering”, *Science*, vol. 330, no. 6009, pp. 1368-1370, Dec. 2010.

[52]H. Kano and H. Hamaguchi, “Supercontinuum dynamically visualizes a dividing single cell.”, *Analytical Chemistry*, vol. 79, no. 23, pp. 8967-73, Dec. 2007.

[53]X. Nan, “Vibrational imaging of lipid droplets in live fibroblast cells with coherent anti-Stokes Raman scattering microscopy”, *The Journal of Lipid Research*, vol. 44, no. 11, pp. 2202-2208, Aug. 2003.

[54]C. Huang, H. Hamaguchi, and S. Shigeto, “In vivo multimode Raman imaging reveals concerted molecular composition and distribution changes during yeast cell cycle”, *Chemical Communications*, vol. 47, no. 33, p. 9423, Jan. 2011.

[55]H. J. Manen, Y. M. Kraan, D. Roos and C. Otto, “Single-cell Raman and fluorescence microscopy reveal the association of lipid bodies with phagosomes in leukocytes”, *Proceedings of the National Academy of Sciences*, vol. 102, no. 29, pp. 10159-10164, Jul. 2005.

[56]H. Wu, J. V. Volponi, A. E. Oliver, A. N. Parikh, B. A. Simmons, S. Singh, H. Wu, J. V. Volponi, A. E. Oliver, A. N. Parikh, B. A. Simmons, and S. Singh, “In vivo lipidomics using single-cell Raman spectroscopy”, *Proceedings of the National Academy of Sciences*, vol. 108, no. 9, pp. 3809-3814, Mar. 2011.

- [57]C. Matthäus, S. Boydston-White, and M. Miljković, “Raman and infrared microspectral imaging of mitotic cells”, *Applied Spectroscopy*, vol. 60, no. 1, pp. 1-8, Nov. 2006.
- [58]H. A. Rinia, K. N. Burger, M. Bonn, and M. Müller, “Quantitative Label-Free Imaging of Lipid Composition and Packing of Individual Cellular Lipid Droplets Using Multiplex CARS Microscopy”, *Biophysical journal*, vol. 95, no. 10, pp. 4908-4914, Nov. 2008.
- [59]M. Manefield, A. S. Whiteley, R. I. Griffiths, and M. J. Bailey, “RNA Stable Isotope Probing, a Novel Means of Linking Microbial Community Function to Phylogeny”, *Applied and Environmental Microbiology*, vol. 68, no. 11, pp. 5367-5373, Nov. 2002.
- [60]S. Radajewski, P. Ineson, N. R. Parekh, J. C. Murrell, and J. C. Parekh, “Stable-isotope probing as a tool in microbial ecology”, *Nature*, vol. 403, no. 6770, pp. 646-649, Feb. 2000.
- [61]N. Jehmlich, F. Schmidt, M. Taubert, J. Seifert, F. Bastida, M. von Bergen, H. Richnow, and C. Vogt, “Protein-based stable isotope probing”, *Nature Protocols*, vol. 5, no. 12, pp. 1957-1966, Nov. 2010.
- [62]S. Haider, M. Wagner, M. C. Schmid, B. S. Sixt, J. G. Christian, G. Häcker, P. Pichler, K. Mechtler, A. Müller, C. Baranyi, E. R. Toenshoff, J. Montanaro, and M. Horn, “Raman microspectroscopy reveals long-term extracellular activity of chlamydiae”, *Molecular Microbiology*, vol. 77, no. 3, pp. 687-700, Aug. 2010.
- [63]W. E. Huang, K. Stoecker, R. Griffiths, L. Newbold, H. Daims, A. S. Whiteley, and M. Wagner, “Raman-FISH: combining stable-isotope Raman spectroscopy and fluorescence in situ hybridization for the single cell analysis of identity and function”, *Environmental Microbiology*, vol. 9, no. 8, pp. 1878-1889, Aug. 2007.
- [64]C. Matthäus, A. Kale, T. Chernenko, V. Torchilin, and M. Diem, “New Ways of Imaging Uptake and Intracellular Fate of Liposomal Drug Carrier Systems inside Individual Cells, Based on Raman Microscopy”, *Molecular Pharmaceutics*, vol. 5, no. 2, pp. 1-7, Jan. 2008.
- [65]P. Carey, *Biochemical applications of Raman and resonance Raman spectrometers*. Academic Press, 1982.
- [66]Y. Min, T. Yamamoto, E. Kohda, and T. Ito and H. Hamaguchi, “1064 nm near-infrared multichannel Raman spectroscopy of fresh human lung tissues”, *Journal of Raman*

Spectroscopy, vol. 36, pp. 73-76, Jan. 2005.

[67]R. Kast, M. Detroit, G. Serhatkulu, A. Cao, A. Pandya, H. Dai, J. Thakur, V. Naik, M. Dearborn, R. Naik, M. Klein, G. Auner, and R. Rabah, "Raman spectroscopy can differentiate malignant tumors from normal breast tissue and detect early neoplastic changes in a mouse model", *Biopolymers*, vol. 89, no. 3, pp. 235-241, Mar. 2008.

[68]Z. Liu, W. Cai, L. He, N. Nakayama, K. Chen, X. Sun, X. Chen, and H. Dai, "In vivo biodistribution and highly efficient tumour targeting of carbon nanotubes in mice", *Nature Nanotechnology*, vol. 2, no. 1, pp. 47-52, Dec. 2006.

[69]S. Keren, C. Zavaleta, Z. Cheng, A. Zerda, O. Gheysens, and S. Gambhir, "Noninvasive molecular imaging of small living subjects using Raman spectroscopy", *Proceedings of the National Academy of Sciences*, vol. 105, no. 15, pp. 5844-5849, Apr. 2008.

[70]C. Zavaleta, B. Smith, I. Walton, W. Doering, G. Davis, B. Shojaei, M. Natan, and S. Gambhir, "Multiplexed imaging of surface enhanced Raman scattering nanotags in living mice using noninvasive Raman spectroscopy", *Proceedings of the National Academy of Sciences*, vol. 106, no. 32, pp. 13511-13516, Aug. 2009.

[71]A. Enejder, T. Seccina, and J. Oh, "Raman spectroscopy for noninvasive glucose measurements", *Journal of Biomedical Optics*, vol. 10, no. 3, pp. 0311141-9, Jun. 2005.

[72]C. Onogi, H. Torii, and H. Hamaguchi, "Raman Spectra of Isotope-substituted Mitochondria of Living Budding Yeast Cells: Possible Origin of the 'Raman Spectroscopic Signature of Life'", *Chemistry Letters*, vol. 38, no. 9, pp. 898-9, Aug. 2009.

[73]L. Chiu, F. Hullin-Matsuda, T. Kobayashi, H. Torii, and H. Hamaguchi, "On the origin of the 1602 cm^{-1} Raman band of yeasts; contribution of ergosterol", *Journal of Biophotonics*, pp. 1-5, Jan. 2012.

[74]T. Czabany, K. Athenstaedt, and G. Daum, "Synthesis, storage and degradation of neutral lipids in yeast", *Biochimica et Biophysica Acta (BBA) - Molecular and Cell Biology of Lipids*, vol. 1771, no. 3, pp. 299-309, Mar. 2007.

[75]V. Barzda, C. Greenhalgh, J. A. der Au, and S. Elmore, "Visualization of mitochondria in cardiomyocytes by simultaneous harmonic generation and fluorescence microscopy", *Optics*

express, vol. 13, no. 20, pp. 8263-8276, Oct. 2005.

[76]H. Segawa, M. Okuno, H. Kano, P. Leproux, V. Couderc and H. Hamaguchi, “Label-free tetra-modal molecular imaging of living cells with CARS, SHG, THG and TSFG (coherent anti-Stokes Raman scattering, second harmonic generation, third harmonic generation and third order sum-frequency generation)”, *Optics Express*, vol. 20, no. 9, pp. 9551-7, Apr. 2012.

[77]R. Singh, S. Kaushik, Y. Wang, Y. Xiang, I. Novak, M. Komatsu, K. Tanaka, A. M. Cuervo, and M. J. Czaja, “Autophagy regulates lipid metabolism”, *Nature*, vol. 458, no. 7242, pp. 1131-1135, Apr. 2009.

[78]A. Matsuyama, R. Arai, Y. Yashiroda, A. Shirai, A. Kamata, S. Sekido, Y. Kobayashi, A. Hashimoto, M. Hamamoto, Y. Hiraoka, S. Horinouchi, and M. Yoshida, “ORFeome cloning and global analysis of protein localization in the fission yeast *Schizosaccharomyces probe*”, *Nature Biotechnology*, vol. 24, no. 7, pp. 841-847, Jun. 2006.

[79]L. McDonnell and R. Heeren, “Imaging mass spectrometry”, *Mass Spectrometry Reviews*, Vol. 26, no. 4, pp. 606-43, Jul. 2007.

